The dynamics of neutrino-driven supernova explosions after shock revival in 2D and 3D

Muller, B. (2015). The dynamics of neutrino-driven supernova explosions after shock revival in 2D and 3D. *Monthly Notices of the Royal Astronomical Society*, *453*, 287-310. https://doi.org/10.1093/mnras/stv1611

Published in:
Monthly Notices of the Royal Astronomical Society

Document Version:
Publisher's PDF, also known as Version of record

Monthly Notices
of the
ROYAL ASTRONOMICAL SOCIETY

MNRAS **453,** 287–310 (2015) doi:10.1093/mnras/stv1611

The dynamics of neutrino-driven supernova explosions after shock revival in 2D and 3D

B. Müller★

Monash Centre for Astrophysics, School of Physics and Astronomy, 19 Rainforest Walk, Monash University, Victoria 3800, Australia

Accepted 2015 July 14. Received 2015 July 13; in original form 2015 June 16

ABSTRACT

We study the growth of the explosion energy after shock revival in neutrino-driven explosions in two and three dimensions (2D/3D) using multi-group neutrino hydrodynamics simulations of an 11.2 $M_\odot$ star. The 3D model shows a faster and steadier growth of the explosion energy and already shows signs of subsiding accretion after one second. By contrast, the growth of the explosion energy in 2D is unsteady, and accretion lasts for several seconds as confirmed by additional long-time simulations of stars of similar masses. Appreciable explosion energies can still be reached, albeit at the expense of rather high neutron star masses. In 2D, the binding energy at the gain radius is larger because the strong excitation of downward-propagating g modes removes energy from the freshly accreted material in the downflows. Consequently, the mass outflow rate is considerably lower in 2D than in 3D. This is only partially compensated by additional heating by outward-propagating acoustic waves in 2D. Moreover, the mass outflow rate in 2D is reduced because much of the neutrino energy deposition occurs in downflows or bubbles confined by secondary shocks without driving outflows. Episodic constriction of outflows and vertical mixing of colder shocked material and hot, neutrino-heated ejecta due to Rayleigh–Taylor instability further hamper the growth of the explosion energy in 2D. Further simulations will be necessary to determine whether these effects are generic over a wider range of supernova progenitors.

Key words: hydrodynamics – instabilities – neutrinos – radiative transfer – supernovae: general.

1 INTRODUCTION

After decades of research, the mechanism powering core-collapse supernovae is still one of the outstanding problems in theoretical astrophysics. The so-called delayed neutrino-driven mechanism currently remains the most popular and best explored explanation (see Janka 2012; Burrows 2013 for current reviews) for 'ordinary' supernova explosions not exceeding $\sim 10^{51}$ erg. In its modern guise, the neutrino-driven mechanism relies on additional support for shock expansion in the form of hydrodynamic instabilities like convection (Burrows & Fryxell 1992; Herant, Benz & Colgate 1992; Herant et al. 1994; Burrows, Hayes & Fryxell 1995; Janka & Müller 1996; Müller & Janka 1997) and the standing accretion shock instability (SASI; Blondin, Mezzacappa & DeMarino 2003; Foglizzo et al. 2007; Laming 2007; Guilet & Foglizzo 2012). Indeed, many successful multi-dimensional simulations of neutrino-driven shock revival (mostly in 2D, i.e. under the assumption of axisymmetry) have strengthened our confidence in the neutrino-driven mechanism over the recent years (Buras et al. 2006b; Marek & Janka 2009; Suwa et al. 2010, 2013; Yakunin et al. 2010; Janka et al. 2012; Müller, Janka & Marek 2012a; Müller, Janka & Heger 2012b; Bruenn et al. 2013; Pan et al. 2015). However, both the long-time evolution of the successful 2D models and the advent of three-dimensional (3D) simulations have revealed two serious challenges for the neutrino-driven paradigm. With the exception of Bruenn et al. (2013), the majority of successful 2D simulations tended to produce explosions that are probably underenergetic. Moreover, the most ambitious self-consistent 3D simulations with multi-group neutrino transport have so far either failed to yield explosions (Hanke et al. 2013; Tamborra et al. 2014a,b) or, in the few successful cases, showed a considerable delay in shock revival (Lentz et al. 2015; Melson et al. 2015a) and significantly smaller explosion energies (Takiwaki, Kotake & Suwa 2014). Only the explosion of a 9.6 $M_\odot$ star recently simulated by Melson, Janka & Marek (2015b) is an exception from this trend. Whether the neutrino-driven mechanism provides a robust explanation for shock revival and can account for the observed explosion properties of core-collapse supernovae may appear doubtful in the light of these results.

There is now an emerging consensus about the reasons underlying the more fundamental problem of missing or delayed explosions in 3D. Both simple light-bulb- and leakage-based simulations (Hanke

★ E-mail: bernhard.mueller@monash.edu

et al. 2012; Couch 2013a,b; Couch & O'Connor 2014; Couch & Ott 2015) as well as models with multi-group transport (Hanke et al. 2013; Takiwaki et al. 2014) find an artificial accumulation of turbulent kinetic energy on large spatial scales in 2D due to the action of the inverse turbulent cascade (Kraichnan 1967). Effectively, the forward cascade in 3D provides for more efficient damping/dissipation of the turbulent motions in the post-shock region, resulting in smaller turbulent kinetic energies. Since the turbulent kinetic energy is directly related to the Reynolds stresses (i.e. loosely speaking, the 'turbulent pressure') that have been identified as the primary agent fostering shock expansion in multi-D (Burrows et al. 1995; Murphy, Dolence & Burrows 2013; Couch & Ott 2015; Müller & Janka 2015), this affects the critical neutrino luminosity $L_{\rm crit}$ (Burrows & Goshy 1993; Murphy & Burrows 2008) required to power an explosive runaway. However, even though the higher explosion threshold in 3D has emerged as a systematic effect, it none the less remains a small effect. Current light-bulb models (Hanke et al. 2012; Couch 2013b; Dolence et al. 2013) invariably show a similar reduction of 20–30 per cent in critical luminosity in 2D/3D compared to 1D, with Dolence et al. (2013) still finding a slightly lower explosion threshold in 3D. Likewise, neutrino hydrodynamics simulations (Hanke et al. 2013; Takiwaki et al. 2014) show very similar heating conditions in 2D and 3D prior to shock revival [and even transient phases with better heating conditions in 3D in Hanke et al. (2013)], although the small differences between 2D and 3D eventually thwart shock revival in the 3D models of Hanke et al. (2013) and Tamborra et al. (2014a,b). Even though the adverse effects of the forward cascade in 3D may still be underestimated by the relatively crude grid resolution that current models can afford (Hanke et al. 2012; Couch 2013b; Abdikamalov et al. 2014), it thus emerges that 3D models of neutrino-driven supernova explosions are very close to the explosion threshold. Consequently, relatively small refinements in the simulations and the initial models may be sufficient to obtain explosions, e.g. *moderate* rotation (Nakamura et al. 2014), magnetic fields (Obergaulinger, Janka & Aloy 2014), asphericities in the progenitor core (Couch & Ott 2013; Couch et al. 2015; Müller & Janka 2015), or modifications to the standard neutrino interaction rates (Melson et al. 2015a). The emergence of the spiral mode of the SASI could even allow strongly SASI-dominated models to explode earlier in 3D than in 2D (Fernández 2015).

By contrast, the problem of underenergetic neutrino-driven explosions in 2D has so far gone without a convincing theoretical explanation, and fewer suggestions have been made to remedy it, although it may be more serious in the sense that it affects even models with *successful* shock revival. While recent analyses of well-observed supernovae (Tanaka et al. 2009; Utrobin & Chugai 2011; Poznanski 2013; Chugai & Utrobin 2014; Pejcha & Prieto 2015) suggest a broader range of explosion energies for Type II-P supernovae within $\sim(0.1-2)\times10^{51}$ erg instead of a single 'canonical' value of 10^{51} erg, there is arguably still a discrepancy, since almost none of the successful 2D and 3D models with multi-group neutrino transport show explosion energies considerably above 10^{50} erg, e.g. the final values at the end of the simulations are a few 10^{49} erg in Marek & Janka (2009) for progenitors with 11.2 and 15 $\mathrm{M}_\odot$, $\lesssim 10^{50}$ erg for a 13 $\mathrm{M}_\odot$ progenitor in Suwa et al. (2010), and 4×10^{49} erg (11.2 $\mathrm{M}_\odot$ progenitor), 1.3×10^{50} erg (15 $\mathrm{M}_\odot$), and 1.3×10^{50} erg (27 $\mathrm{M}_\odot$) in Janka et al. (2012). Moreover, these estimates are not corrected for the 'overburden', i.e. the binding energy of the layers outside the shock, so that it remains unclear whether the explosions become energetic enough to shed the envelope at all. At first glance, the low explosion energies may simply be due to the fact that the simulations typically terminate before the explosion energy reaches its asymptotic value. While it can be argued that the final explosion energies may yet be higher by a factor of several because continued accretion sustains strong neutrino emission after shock revival that can power outflows from the gain region for $\gtrsim$0.5 s, this assumption creates several other problems. Sustained accretion over $\gtrsim$0.5 s might shift the resulting remnant mass distribution well above the average birth mass of neutron stars $M_{\rm grav}\approx1.35\,\mathrm{M}_\odot$ (Schwab, Podsiadlowski & Rappaport 2010) inferred from observations (which may, however, suffer from a selection bias). Only the 2D models of Bruenn et al. (2014) form an exception from this trend; they obtain explosion energies in the range of (3.4–8.8) $\times$ 10^{50} erg for progenitors between 12 and 25 $\mathrm{M}_\odot$ as well as reasonable nickel masses.

While this is encouraging, explosion energies above 10^{51} erg still remain unexplained, and the problem of underenergetic supernova explosion will arguably still linger as long as the discrepancies between the different simulation codes are not resolved. Interestingly, Melson et al. (2015b) recently reported that 3D effects, while apparently detrimental for shock revival in more massive progenitors, actually boost the explosion energy in a 9.6 $\mathrm{M}_\odot$ progenitor by $\sim$10 per cent by reducing the infall velocity in the accretion downflow and hence the cooling below the gain layer. Here, we further investigate their intriguing premise that 3D effects, while hurtful for shock revival, can prove beneficial in other situations and contribute to solving the problem of low explosion energies.

In this paper, we present a successful 3D multi-group neutrino hydrodynamics simulation of an 11.2 $\mathrm{M}_\odot$ progenitor with the COCONUT-FMT code (Müller, Janka & Dimmelmeier 2010; Müller & Janka 2015) as further evidence that 3D turbulence plays a positive role *after* the onset of the explosion. By comparing the dynamics and energetics of the 3D explosion model to several long-time simulations of 2D progenitors in the mass range between 11 and 11.6 $\mathrm{M}_\odot$, we demonstrate how 3D effects can lead to a faster, more robust growth of the explosion energy provided that shock revival can be achieved. So far, the long-time effects of the dimensionality during the first hundreds of milliseconds to seconds after shock revival have received less attention than the role of the third dimension in shock revival. Successful first-principle models are still scarce and cannot be evolved for a sufficiently long time yet to address this phase in detail, while light-bulb-based studies of supernova energetics in 2D and 3D (Handy, Plewa & Odrzywołek 2014) cannot adequately account for the feedback of the subsiding accretion on to the neutrino heating and do not show the drawn-out long-time accretion characteristic of first-principle models. In this paper, we show that this phase deserves a closer look.

Our paper is structured as follows. In Section 2, we review the numerical methods for hydrodynamics and neutrino transport used in our version of the COCONUT code, including a brief sketch of the modifications used in the 3D version. In Section 3, we first give a descriptive overview of the differences in shock propagation and explosion properties between the 2D and 3D models. Since the question of shock revival in 3D is not the objective of our current study, we only provide a brief, cautionary assessment of shock revival in the 3D model against the backdrop of recent first-principle models in Section 4. In Section 5, we then analyse the physical effects underlying these differences by combining a separate analysis of the outflows and downflows in the spirit of Melson et al. (2015b). Finally, we summarize our results and discuss their implications in Section 6.

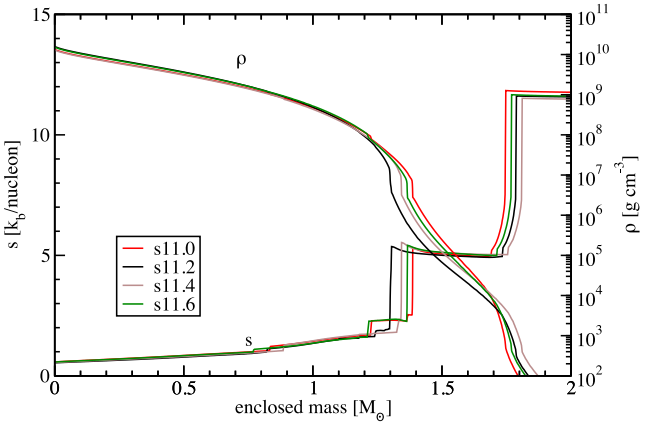

Figure 1. Density ρ and entropy s for the four progenitors s11.0 (red), s11.2 (black), s11.4 (light brown), and s11.6 (green) as a function of enclosed mass.

2 NUMERICAL METHODS AND MODEL SETUP

2.1 Progenitor models

We simulate the collapse and post-bounce phase of the (non-rotating) 11.2 $M_\odot$ solar-metallicity progenitor s11.2 of Woosley, Heger & Weaver (2002) in 2D and 3D. In order to gauge the effect of stochastic model variations, we perform two different 2D simulations (s11.2_2Da and s11.2_2Db[1]) for this progenitor, and we also conduct simulations for three other solar-metallicity progenitors of Woosley et al. (2002) with similar zero-age main-sequence (ZAMS) mass and density structure (11, 11.4, 11.6 $M_\odot$). We randomly perturb the radial velocity v_r at the beginning of collapse using a perturbation amplitude $\delta v_r/v_r = 10^{-5}$.

In Fig. 1, we show density and entropy profiles for the four progenitors simulated in the different 2D and 3D runs. Despite small differences in the location of the interfaces between the different shells, the models are very similar in terms of structure with a pronounced density jump between the silicon shell and the convective shell above the active oxygen burning zone. As we shall see, the 2D models of the different progenitors are qualitatively very similar in terms of explosion dynamics and energetics and should thus illustrate the generic behaviour of supernova explosions originating from progenitors in this mass range.

2.2 Numerical methods

The simulations are performed with the general relativistic (GR) neutrino hydrodynamics code COCONUT (Dimmelmeier, Font & Müller 2002; Müller et al. 2010; Müller & Janka 2015). Our version of COCONUT uses piecewise parabolic reconstruction (Colella & Woodward 1984) combined with a hybrid HLLC/HLLE Riemann solver (Mignone & Bodo 2005) to obtain higher order spatial accuracy. COCONUT employs spherical polar coordinates (r, θ, φ), which leads to strong time-step constraints near the polar axis in 3D due to the converging grid geometry. We circumvent this problem using an adapted version of the mesh coarsening scheme of Cerdá-Durán (2009). While the equations of hydrodynamics are solved on a fine grid with constant spacing $\delta\varphi$ in longitude everywhere, a filter is applied to the solution after each time step to remove short-wavelength noise in the φ-direction by projecting the conserved variables on to piecewise linear/quadratic[2] functions in 'supercells' that contain $2^{n(\theta)}$ fine cells in the φ-direction. The projection algorithm is implemented conservatively, and the slopes for the filtered solution are obtained using the monotonized-central limiter of van Leer (1977). The supercell size $2^{n(\theta)}$ is chosen such that $n\sin\theta > 1/2$ is maintained at any latitude. This ensures that the allowed CFL time step at high latitudes is at most shorter by a factor of $\sim$2 compared to the equatorial region, and limits the filtering to a region of 30° around the pole, which corresponds to 13.3 per cent of the total volume. Similar techniques have long been used in numerical meteorology, cp. Kageyama & Sato (2004) and chapter 18 in Boyd (2001). Polar filtering allows us to maintain the same effective angular resolution of 1°.4 in 2D and 3D with grids of $N_r \times N_\theta = 550 \times 128$ zones (2D) and $N_r \times N_\theta \times N_\varphi = 550 \times 128 \times 256$ zones (3D, fine grid) covering the innermost 10^5 km of the star, respectively.

Like any other solution to avoid the coordinate singularity and the excessive time-step constraint near the axis such as Cartesian coordinates, overset grids (Kageyama & Sato 2004; Wongwathanarat, Hammer & Müller 2010; Melson, Janka & Marek 2015b), or cubed-sphere grids (Ronchi, Iacono & Paolucci 1996; Koldoba et al. 2002; Zink, Schnetter & Tiglio 2008; Fragile et al. 2009), this polar filtering procedure has specific advantages and disadvantages. Unlike Cartesian codes, polar filtering allows us to maintain spherical symmetry in the initial conditions and explicit symmetry-breaking terms can be avoided. Different from cubed-sphere grids, the grid remains orthogonal, and global conservation laws are easier to enforce than for overlapping overset grids. On the other hand, projecting the solution to piecewise linear function effectively introduces an anisotropy in the numerical viscosity and diffusivity (an unwelcome effect that is minimized by overset or cubed-sphere grids but also manifests itself for Cartesian grids that are prone to the development of $m = 4$ modes).

The space–time metric is computed using the extended conformal flatness condition (xCFC; Cordero-Carrión et al. 2009). Because the asphericities in the gravitational field are small for non-rotating core-collapse supernovae, we use the monopole approximation for the gravitational field, i.e. the lapse function α, the conformal factor ϕ, and the radial component β_r of the shift vector only depend on r, and the non-radial components β_θ and β_φ of the shift vector are set to zero.

For the neutrinos, we use the fast multi-group transport (FMT) scheme of Müller & Janka (2015), which is based on a stationary two-stream solution of the relativistic transfer equation that is combined with an analytic variable Eddington factor closure at low optical depths. This scheme includes GR effects under the assumption of a stationary metric, but neglects velocity-dependent effects like

[1] Scattering on nuclei (including α-particles) was switched off after bounce for model s11.2_2Db, which leads to minor changes in early shock propagation, but is inconsequential for the long-time evolution. Since the energy exchange due to recoil in neutrino–nucleon scattering was taken to be proportional to the total scattering opacity instead of the neutrino–nucleon scattering opacity only (see equation A31 in Müller & Janka 2015) in model s11.2_2Da and all other models, the runs with neutrino scattering on nuclei overestimate pre-heating from heavy flavour neutrinos outside the shock during the early post-bounce phase (whereas nuclei actually receive negligible recoil in scattering reactions), which leads to a slight reduction of the heavy flavour neutrino luminosity and a slightly slower contraction of the proto-neutron star compared to s11.2_2Db.

[2] For example, we use linear functions for the Eulerian density D and the mass fractions X_i so that the conserved partial masses DX_i are represented by quadratic functions.

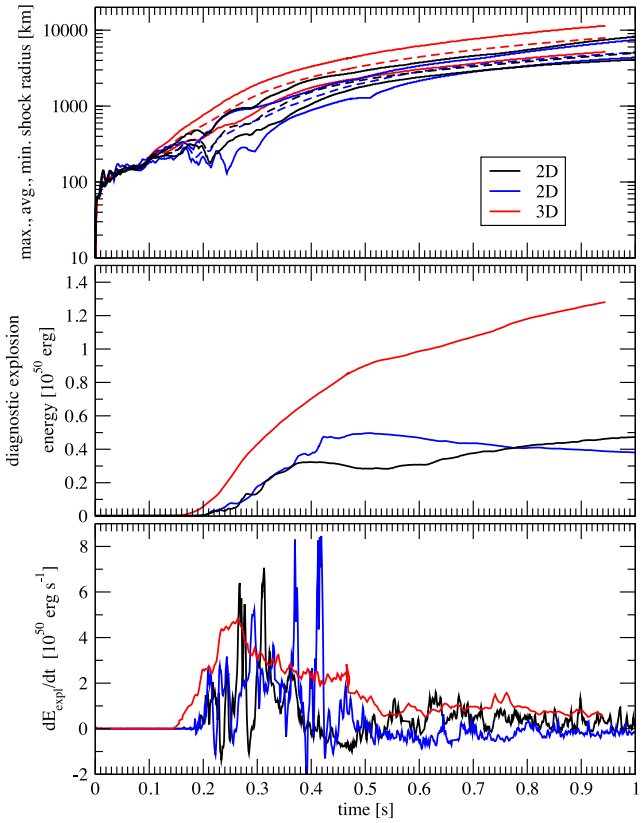

Figure 2. Shock propagation and diagnostic explosion energy $E_{\rm expl}$ for the 11.2 $M_\odot$ progenitor in 2D and 3D. The top panel shows the maximum, minimum (solid), and average (dashed) shock radius for model s11.2_2Da (black), s11.2_2Db (blue), and s11.2_3D (red). The middle and bottom panels show the diagnostic explosion energy $E_{\rm expl}$ and its time derivative $\mathrm{d}E_{\rm expl}/\mathrm{d}t$.

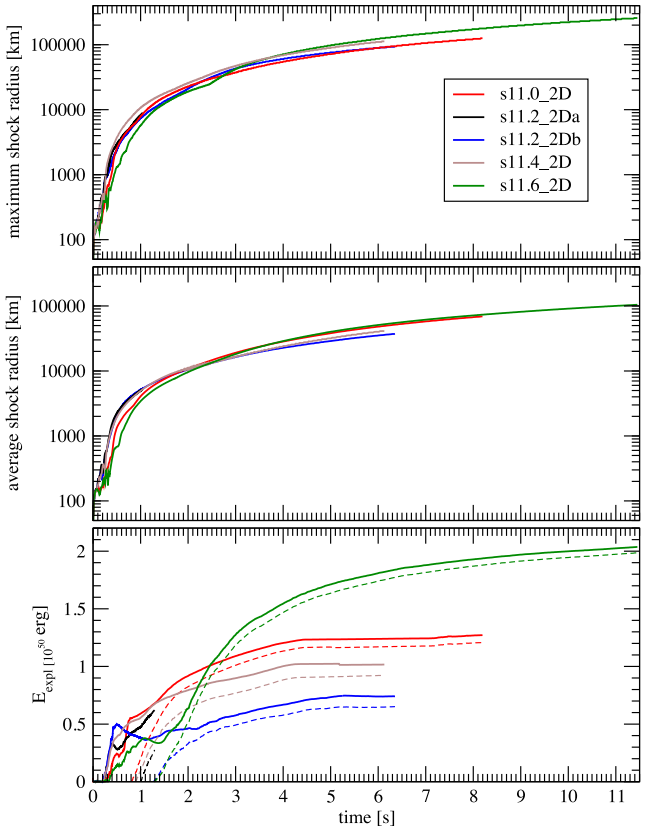

Figure 3. Shock propagation and diagnostic explosion energy $E_{\rm expl}$ for the different progenitors in 2D. The top and middle panels show the maximum and average shock radius, respectively. The bottom panel shows the diagnostics explosion energy $E_{\rm expl}$ as a function of time (solid lines). Dashed lines show the time evolution $E_{\rm expl} - E_{\rm ov}$, i.e. the diagnostic energy corrected for the binding energy (overburden) $E_{\rm ov}$ of the material ahead of the shock. Red, black, blue, light brown, and green curves are used for models s11.0_2D, s11.2_2Da, s11.2_2Db, s11.4_2D, and s11.6_2D.

Doppler shift and aberration. The neutrino rates include emission, absorption, and elastic scattering by nuclei and free nucleons [along the lines of Bruenn (1985)] as well as an effective one-particle rate for nucleon–nucleon bremsstrahlung and an approximate treatment of the energy exchange in neutrino–nucleon scattering reactions. Comparisons of the FMT scheme with the more sophisticated relativistic neutrino transport solver VERTEX (Rampp & Janka 2002; Müller et al. 2010) showed excellent qualitative and good quantitative agreement. For more details, we refer the reader to Müller & Janka (2015).

In order to further alleviate the time-step constraint, the innermost part of the computational domain (where densities exceed $\sim 5 \times 10^{11}$ g cm^{-3}) is calculated in spherical symmetry using a conservative implementation of mixing-length theory for proto-neutron star convection, a procedure that has been used in the context of supernova simulations before (e.g. Wilson & Mayle 1988; Hüdepohl 2014). The transition density is adjusted such that it lies inside the convectively stable cooling layer.

In the high-density regime, we use the equation of state (EoS) of Lattimer & Swesty (1991) with a bulk incompressibility modulus of nuclear matter of $K = 220$ MeV. At low densities, we employ an EoS accounting for photons, electrons, and positrons of arbitrary degeneracy, an ideal gas contribution from baryons (nucleons, protons, α-particles, and 14 other nuclear species). Nuclear reactions are treated using 'flashing' as described in Rampp & Janka (2002).

3 OVERVIEW OF SIMULATION RESULTS

In all our simulations, runaway shock expansion sets in when the Si/SiO interface reaches the shock and the mass accretion rate drops rapidly. Figs 2 (all 2D/3D 11.2 $M_\odot$ models) and 3 (long-time evolution of all 2D models) provide an overview over the propagation of the shock and the growth of the explosion energies for the different models; they show the maximum, minimum (only Fig. 2), and angled-averaged shock radius, as well as the 'diagnostic explosion energy' $E_{\rm expl}$, which we define as the total net energy (i.e. gravitational+internal+kinetic energy) of all the material that is nominally unbound and is moving outwards with positive radial velocity at a given time (cp. Müller et al. 2012a; Bruenn et al. 2014). The nucleon rest masses are not included in the internal energy, i.e. nucleon recombination only contributes to the diagnostic energy once it actually takes places. Fig. 2 also shows the time derivative of the diagnostic energy. Key results of the simulations, including the diagnostics energy and the baryonic remnant mass at the end of the simulations as well as estimates for the final remnant mass (see Section 3.3 below), are given in Table 1.

3.1 Differences between 2D and 3D during the first second

For the 11.2 $M_\odot$ progenitor, the first second after bounce is shown in detail in Fig. 2 both in 2D and 3D. In addition, Figs 4 and 5 illustrate

Table 1. Overview of simulations. The extrapolation of the final remnant masses (last column) is discussed in Section 3.3.

Model	Progenitor	Dimensionality	Post-bounce time reached (s)	Diagnostic energy reached (erg)	Baryonic neutron star mass reached ($M_\odot$)	Extrapolated baryonic remnant mass ($M_\odot$)
s11.0_2D	s11.0	2	8.195	1.3×10^{50}	1.62	1.62
s11.2_3D	s11.2	3	0.944	1.3×10^{50}	1.33	1.48
s11.2_2Da	s11.2	2	1.044	5.0×10^{49}	1.37	–
s11.2_2Db	s11.2	2	6.003	7.8×10^{49}	1.47	1.69
s11.4_2D	s11.4	2	6.129	1.0×10^{50}	1.56	1.63
s11.6_2D	s11.6	2	11.453	2.1×10^{50}	1.62	1.63

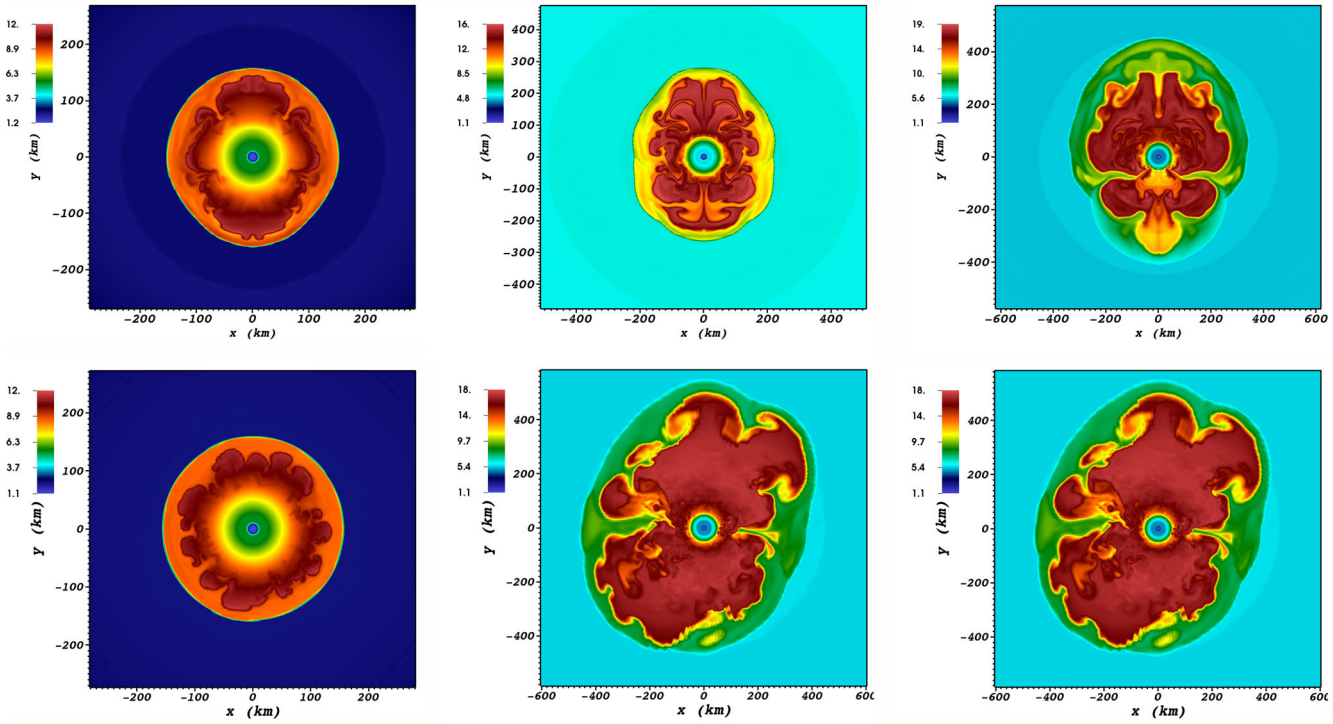

Figure 4. Specific entropy for model s11.2_2Da (top row) and model s11.2_3D (in a slice almost perpendicular to the equatorial plane, bottom row) at post-bounce times of 80, 140, and 181 ms (left to right). Note that a different colour scale for the entropy is used for each of these snapshots.

the multi-dimensional flow morphology for models s11.2_2Da and s11.2_3D on meridional slices, and 3D ray-cast images of neutrino-heated convective bubbles in model s11.2_3D before and after shock revival are shown in Fig. 6.

Prior to the infall of the Si/SiO interface, we find very similar shock trajectories independent of dimensionality. However, prompt convection develops slightly differently in 2D and 3D, and its residual effect on the entropy and lepton number profiles leads to a slight divergence between the 2D and 3D models already at early times in many quantities (neutron star radius, gain radius, cooling profiles, etc.). This effect is not unphysical *per se*, but is most probably exaggerated in our models because the FMT scheme tends to overestimate the strength of prompt convection. In view of the large systematic effects that we shall discuss later, it is also inconsequential, but needs to be borne in mind when comparing the different models.

After the infall of the Si/SiO interface, the shock expands slightly faster in 3D than in 2D, and the explosion energy starts to reach appreciable positive values several tens of milliseconds earlier. Snapshots of the entropy for models s11.2_3D and s11.2_2Da during this phase can be seen in the middle and right columns of Fig. 4, which show the development of large convective plumes in both cases. The reader will note that the plumes are somewhat aligned with the coordinate axis in 3D, which is clearly a result of the coordinate choice but need not be considered harmful as discussed in Section 4. At later times, the morphology of the 3D model is quite different; instead of the broad, laminar downflows characteristic for 2D explosions, the interface between the downflows and the hot, neutrino-heated ejecta eventually becomes turbulent during the infall, resulting in corrugated downflows and partial mixing with the neutrino-heated ejecta, as can be seen most perspicuously in the middle column of Fig. 5.

Soon after shock revival, the 2D models start to go through episodes of halting shock expansion or even transient shock recession. While the growth rate $dE_{\rm expl}/dt$ of the diagnostic explosion energy reaches values comparable to 3D for 100–200 ms, the explosion energy grows much less steadily in the long term and has reached only (4–5) $\times$ 10^{49} erg after 1 s. By contrast, the 3D model shows a steady growth of the explosion energy (1.3×10^{50} erg by the end of the simulation), and considerably faster shock expansion. As illustrated by the mass shell trajectories in Fig. 7, the spherically averaged radial velocity behind the shock becomes positive about

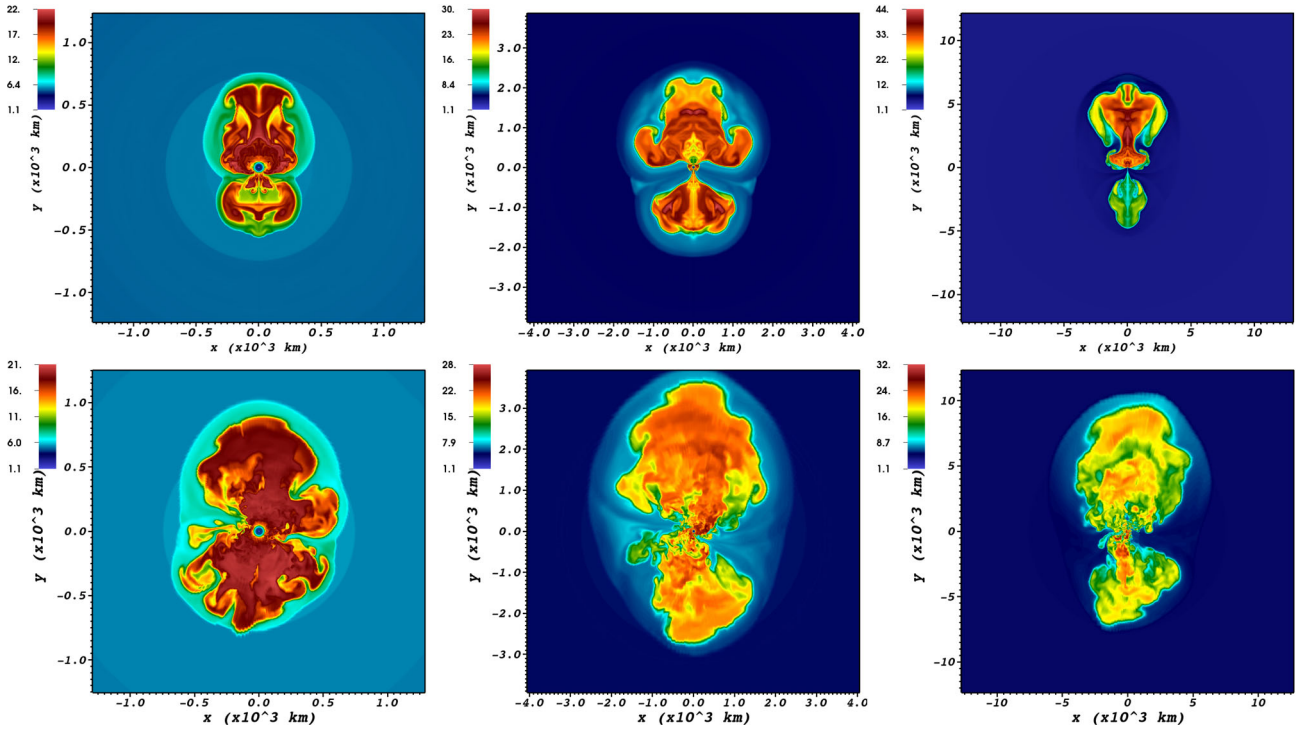

Figure 5. Specific entropy for model s11.2_2Da (top row) and model s11.2_3D (in a slice almost perpendicular to the equatorial plane, bottom row) at post-bounce times of 241, 471, and 944 ms (left to right). Note that a different colour scale for the entropy is used for each of these snapshots.

300 ms after bounce, and the mass shells shocked later than 500 ms after bounce appear to move outwards steadily instead of eventually falling back on to the proto-neutron stars.

3.2 Shock propagation during the first seconds

Before we attempt to extrapolate the final remnant masses, it is useful to point out a simple analytic relation between the diagnostic energy and the shock velocity. During the later phases of the explosion when the explosion energy has saturated, simple analytic models (Sedov 1959; Kompaneets 1960; Laumbach & Probstein 1969; Klimishin & Gnatyk 1981; Koo & McKee 1990; Matzner & McKee 1999) provide a useful qualitative description of shock propagation in hydrodynamical simulations (Woosley & Weaver 1995; Kifonidis et al. 2003; Wongwathanarat, Müller & Janka 2015). These underlying models typically rely on the assumption of self-similarity and/or exponential or power-law approximations for the envelope, neglect the effect of gravity, do not account for continuous energy input into the ejecta, and have been derived under the assumption of spherical symmetry. During the first seconds covered in our simulations, all these conditions are violated. It is remarkable that the approximate formula of Matzner & McKee (1999),

$$v_{\rm sh,MM} = 0.794\sqrt{\frac{E_{\rm expl}}{m}}\left(\frac{m}{\rho_{\rm pre}r^3}\right)^{0.19}, \quad (1)$$

none the less provides a reasonable estimate for the shock velocity $v_{\rm sh}$ already a few hundreds of milliseconds after shock revival if it is evaluated using appropriate definitions for the explosion energy $E_{\rm expl}$, the 'ejecta' mass m, and the pre-shock density $\rho_{\rm pre}$. We find that equation (1) works well if $v_{\rm sh}$ is taken to be the angle-averaged shock velocity, i.e. the time derivative of the angle-averaged shock radius $r_{\rm sh,\,avg}$, if the pre-shock density is evaluated at $r_{\rm sh,\,avg}$, if $E_{\rm expl}$ is identified with the time-dependent diagnostics energy, and if the 'ejecta' mass includes the *entire* mass enclosed by the shock from above and the gain radius from below [and thus cannot properly be termed 'ejecta' mass as in the original work of Matzner & McKee (1999)]. This is illustrated in Fig. 8, which shows the ratio of the angle-averaged shock velocity $v_{\rm sh}$ to the analytic estimate $v_{\rm sh,\,MM}$ of Matzner & McKee (1999). While there is considerable scatter, the numerical models fall in a band with $1 < v_{\rm sh}/\,v_{\rm sh,\,MM} < 1.6$ most of the time, especially at time later than 1 s after bounce. Our models suggest $v_{\rm sh} = 1.3 v_{\rm sh,\,MM}$ as a good analytic estimate for early shock propagation in core-collapse supernovae.

3.3 Explosion energies and neutron star masses

Although the explosion energy in model s11.2_3D has not yet reached its final value and there is still some accretion on to the proto-neutron star, there is no doubt that the incipient explosion will eventually expel the envelope. This is not only clear from the steady outward movement of the shocked mass shells at late times visible in Fig. 7 and in the velocity profiles depicted in Fig. 9; the diagnostic explosion energy is also significantly higher than the residual binding energy of the pre-shock matter [the 'overburden' in the terminology of Bruenn et al. (2013, 2014)] of 5×10^{49} erg. This is clearly different from models s11.2_2Da and s11.2_2Db and the similar 2D explosion models of the same progenitor discussed in Buras et al. (2006b), Marek & Janka (2009), and Müller et al. (2012a).

None the less, the long-time simulations of the 2D models over several seconds show that even such supposedly tepid models eventually develop steady shock propagation and reach sufficiently high diagnostic explosion energies to shed the envelope (Fig. 1). For the low-mass progenitors simulated here, the outgoing and infalling mass shells inevitably separate as the post-shock velocities behind the entire shock front become positive once it reaches the edge of

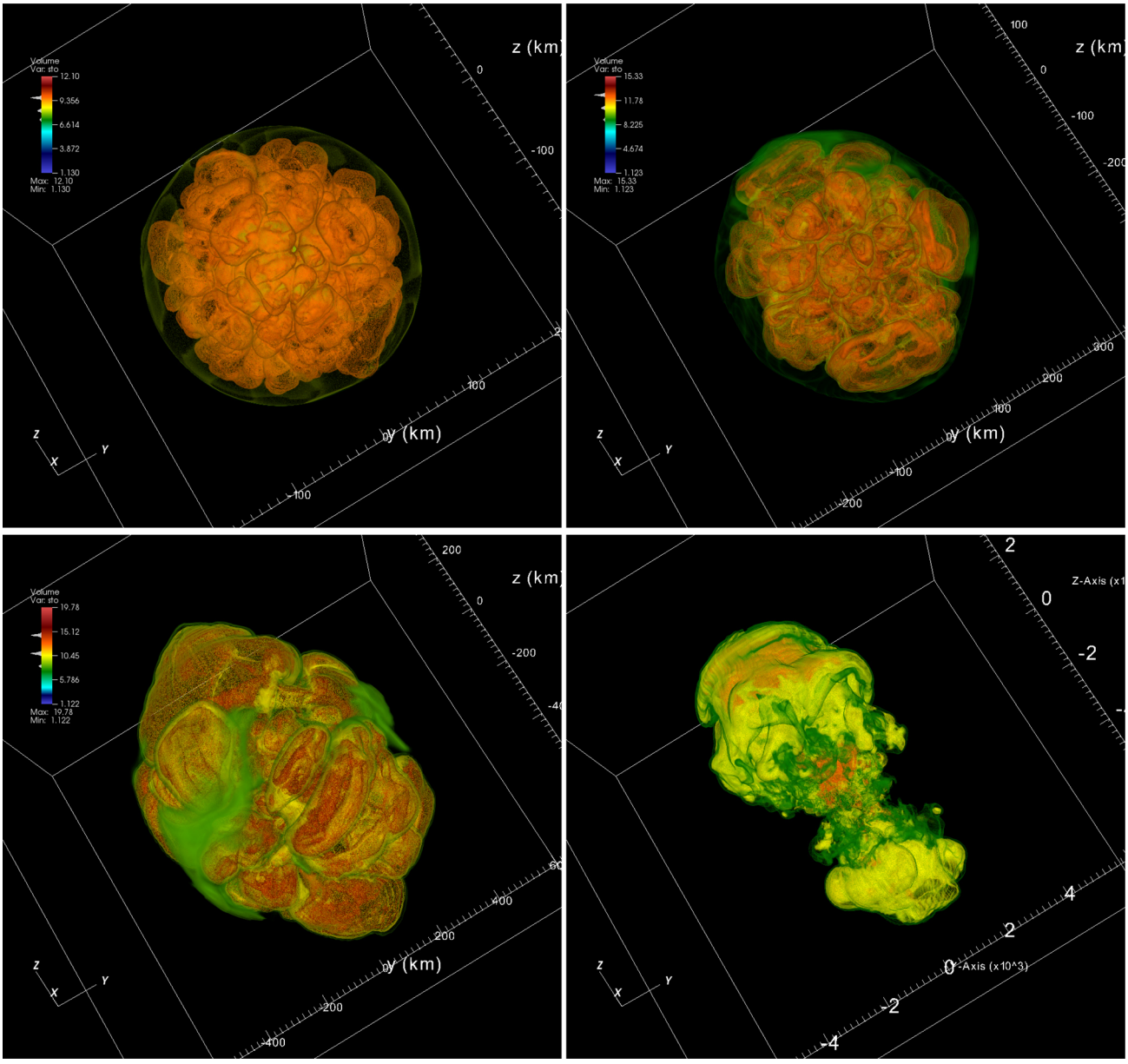

Figure 6. Volume rendering of the entropy in model s11.2_3D at post-bounce times of 89 ms (top left), 134 ms (top right), 210 ms (bottom left), and 580 ms (bottom right).

the relatively small C/O core (1.7–1.8 $M_\odot$), which happens already after a few seconds in these models. The acceleration of the shock at the steep density gradient between the C/O core and the He shell and the small binding energy of the He shell then result in a steady outward movement of the shocked matter. At that point, the overburden of the unshocked envelope becomes almost negligible (e.g. 10^{49} erg for s11.2_2Db, 5×10^{48} erg for s11.6_2D), and we can determine relatively firm lower limits for the final explosion energy.

Continuous accretion over several seconds provides for sufficient neutrino heating to power outflows and pump additional energy into the ejecta over this long time-scale, albeit at a rather modest rate. As a result, models that appear woefully underenergetic during the first second can still develop appreciable explosion energies, the best example being the 11.6 $M_\odot$ model, where $E_{\rm expl}$ grows from 3.5×10^{49} erg at 1 s to 2.0×10^{50} erg after 11 s. The explosion energies obtained after several seconds are comparable to the 3D case and compatible with supernova explosion energies at the lower end of the observed spectrum (see, e.g., Pejcha & Prieto 2015).

The fact that the diagnostic explosion energies increase more or less steadily over several seconds in the 2D models (except for transient phases where the explosion geometry changes because a neutrino-driven outflow is shut off as discussed in Section 5.2.4) has important implications for the usefulness of the diagnostic energy as a predictor of the final explosion properties. On the basis of artificial 1D explosions of Perego et al. (2015), they have recently pointed out that the diagnostic energy *overshoots* the final explosion energy and only approaches its asymptotic value very slowly on a time-scale of seconds, and suggest that a better estimate for the final explosion energy can be obtained by subtracting the overburden $E_{\rm ov}$, i.e. the binding energy of the mass shells outside the shock, from $E_{\rm expl}$. As illustrated by the comparison of $E_{\rm expl}$ and $E_{\rm expl} - E_{\rm ov}$ in Fig. 3, our 2D models show a somewhat different behaviour; similar

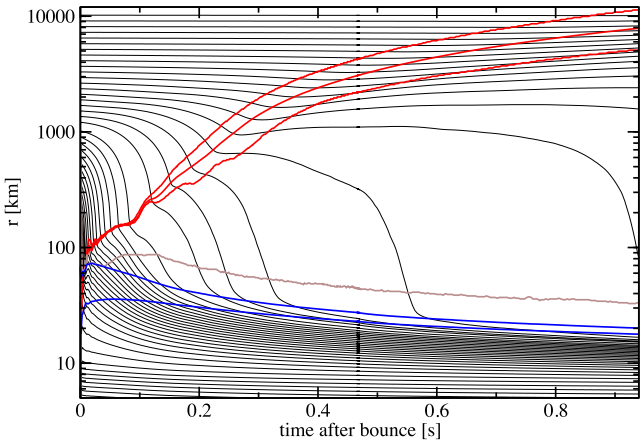

Figure 7. Selected mass shell trajectories (black) for model s11.2_3D computed from spherically averaged density profiles. The trajectories start with roughly equal spacing in log r shortly before bounce. The plot also shows the maximum, average, and minimum shock radius (red), the gain radius (light brown), and the radii corresponding to densities of 10^{11} and 10^{12} g cm^{-3} (blue).

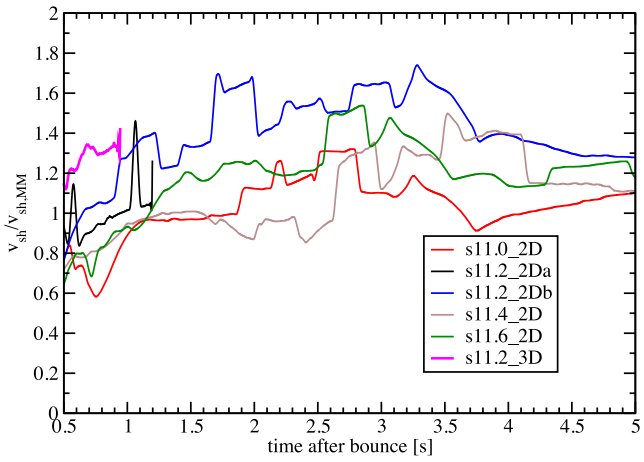

Figure 8. Ratio $v_{\rm sh}/v_{\rm sh,\,MM}$ between the angle-averaged shock velocity $v_{\rm sh} = {\rm d}r_{\rm sh,\,avg}/{\rm d}t$ and the shock velocity $v_{\rm sh,\,MM} = 0.794(E_{\rm expl}/M_{\rm expl})^{1/2}[M_{\rm expl}/(\rho_{\rm pre}r^3)]^{0.19}$ predicted by the model of Matzner & McKee (1999). Note that $r_{\rm sh,\,avg}$ and its numerical derivatives need to be smoothed considerably to allow for a useful comparison. $v_{\rm sh}/v_{\rm sh,\,MM}$ is only shown until 5 s after bounce because the automatic smoothing procedure becomes ineffective towards the end of simulations s11.0_2D, s11.2_2Db, and s11.4_2D and $v_{\rm sh}/v_{\rm sh,\,MM}$ becomes highly oscillatory.

to the simulations of Bruenn et al. (2014), there is no overshooting of $E_{\rm expl}$ above its prospective final value for which it appears to furnish a lower bound rather than an upper bound. This is the result of a fundamentally different way to power the explosion in multi-D compared to 1D. Once an explosion is triggered in 1D, the outflow rate quickly drops and only a weak neutrino-driven wind can still pump energy into the ejecta over time-scales of seconds. The accumulation of shocked material with negative total energy therefore quickly dominates the total energy budget of the ejecta region and $E_{\rm expl}$ decreases, while $E_{\rm expl} - E_{\rm ov}$ remains roughly constant by virtue of total energy conservation. The case for $E_{\rm expl} - E_{\rm ov}$ as a more compelling predictor of the final explosion energy is weaker in multi-D, however, where neutrino-driven outflows can continuously pump energy into the ejecta at a high rate, and a considerable part of the shocked material with negative total energy

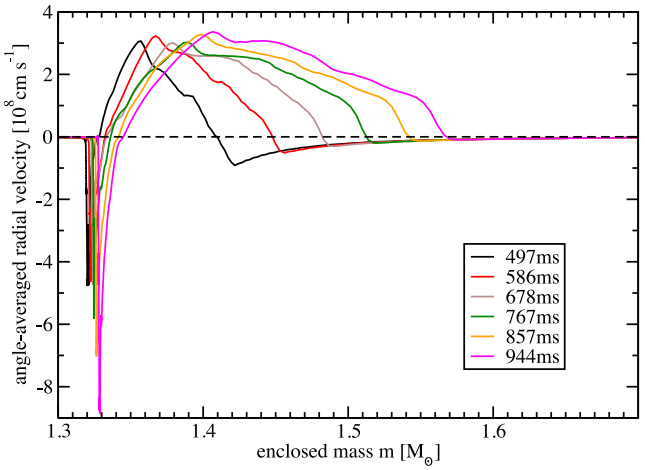

Figure 9. Angle-averaged, density-weighted velocity profiles for model s11.2_3D at different post-bounce times. At the end of the simulation, the angle-averaged velocity is positive outside a mass coordinate of 1.35 $M_\odot$, but the zero-point is still moving outwards in mass. Note that the angle average extends over the post-shock and pre-shock region and cannot be used to infer the post-shock velocity directly.

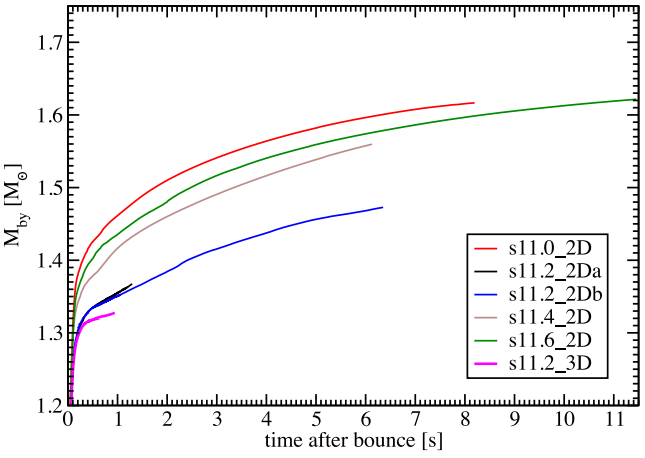

Figure 10. Baryonic neutron star masses (comprising all matter at densities higher than 10^{11} g cm^{-3}) for the different 2D and 3D simulations as a function of time.

is channelled on to the proto-neutron star instead of being swept along by the ejecta and reducing the diagnostic energy. $E_{\rm expl}$ may still decrease somewhat on time-scales longer than 5–10 s as the shock propagates through the helium shell, and this introduces a residual uncertainty of up to ∼15 per cent in the final explosion energy, which we expect to lie in the range bracketed by $E_{\rm expl}$ and $E_{\rm expl} - E_{\rm ov}$. It is also noteworthy that $E_{\rm expl} - E_{\rm ov}$ does not appear to be a good predictor for the final explosion energy at early times simply because its rise phase is much more drawn out than in artificial 1D explosions and it only becomes positive ∼1 s after bounce or later.

While our simulations reach final explosion energies of the order of 10^{50} erg, this comes at the expense of rather high neutron star masses. Fig. 10 shows that the baryonic neutron star masses $M_{\rm by}$ in the 2D models all end up at values $\gtrsim 1.47\,M_\odot$ and will definitely exceed 1.6 $M_\odot$ in cases like s11.0_2D and s11.6_2D. Unless selection effects favour the production of less massive neutron stars in binary systems for some reason, this potentially presents a serious conflict with the inferred neutron star mass distribution. Even if the lowest-mass neutron stars are presumed to originate from electron-capture

supernovae, the masses of the neutron stars in the 2D models would end up well above the mean value of inferred baryonic masses of $1.5\,M_\odot$ (Schwab et al. 2010). Since the simulated models represent progenitors with relatively small cores and a relatively early onset of the explosion, this is highly problematic. It is interesting to note that the 2D models of Bruenn et al. (2014) also show such a tendency towards high neutron star masses despite their relatively high explosion energies (although this tendency is less striking than in our long-time simulations), with $M_{\rm by} = 1.461\,M_\odot$ for their $12\,M_\odot$ model B12-WH07 and values well above $1.6\,M_\odot$ for the three remaining simulations.

The faster rise of the explosion energy in 3D could help to resolve this discrepancy. Although the neutron star mass has not yet converged to a final value, the spherically averaged velocity profiles in Fig. 9 indicate that the final 'mass cut' is slowly emerging. At the end of the simulation, the net mass accretion rate on to the neutron star in s11.2_3D is lower by a factor of $\sim$2 compared to the corresponding 2D models.

To obtain a quantitative estimate for the final neutron star mass, we follow Marek & Janka (2009), who argued that accretion must subside once the post-shock velocity $v_{\rm post}$ becomes comparable to the escape velocity $v_{\rm esc}$. For a strongly asymmetric explosion geometry, $v_{\rm post}$ is of course strongly direction dependent. Hence, material ahead of the neutrino-heated plumes originating from a given mass coordinate m in the progenitor will be accelerated to a higher post-shock velocity by the shock than material with the same initial m that is hit later in a direction where the shock expands more slowly, so that the actual 'mass cut' does not correspond to a single mass shell m in the progenitor. Instead, the dividing line in initial mass coordinate will depend on angle. None the less, one can argue that the criterion $v_{\rm post} = v_{\rm esc}$ still yields a fairly reliable estimate for the final mass of the neutron star if an appropriate spherical average for $v_{\rm post}$ is used.

Equation (1) for the average shock velocity allows us to extrapolate the evolution of the $v_{\rm post}$ if necessary to estimate a spherically averaged 'mass cut'.[3] If the pre-shock velocity is assumed to be negligible, the post-shock velocity becomes

$$v_{\rm post} = \frac{\beta - 1}{\beta} v_{\rm sh}, \tag{2}$$

in terms of the ratio β of the post- and pre-shock density, and equating this to the escape velocity yields the criterion

$$\frac{\beta - 1}{\beta} v_{\rm sh} = \sqrt{\frac{2\,G(M_{\rm by} + M_{\rm gain})}{r}}, \tag{3}$$

where we include the entire mass interior to the shock and not just the mass of the neutron star when computing the escape velocity. At late stages, the compression ratio β typically drops below the value $\beta = 7$ for a radiation-dominated ideal gas with adiabatic index $\gamma = 4/3$ because of nuclear burning and/or because the strong shock approximation is not strictly applicable over the downflows. We therefore compare $v_{\rm sh}$ in model s11.2_3D to the critical velocity $\beta/(\beta - 1)v_{\rm esc}$ for two different values of β in Fig. 11. Fig. 11 suggests a final baryonic remnant mass of 1.41–1.48 $M_\odot$ for s11.2_3D (to which late-time fallback might be added). This would imply that the shock has already passed the initial mass cut in some directions. Estimates along the same lines for the long-time simulations in 2D yield baryonic remnant masses of 1.62 $M_\odot$ for s11.0_2D, 1.63 $M_\odot$ for s11.4_2D, 1.69 $M_\odot$ for s11.0_2Db, and 1.63 $M_\odot$ for s11.6_2D assuming $\beta = 4$.

[3] Equation (1) is also more convenient to use from the numerical point of view because the computation of the shock velocity as a numerical derivative of the shock position typically yields very noisy results.

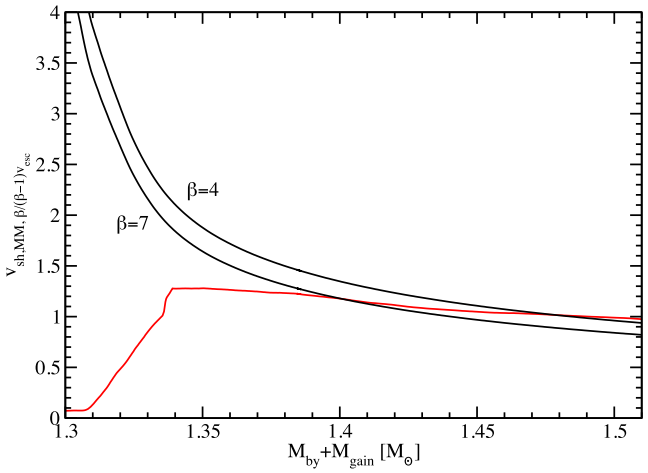

Figure 11. Comparison of the post-shock velocity computed from equation (1) (red curve) to the required shock velocity $\beta/(\beta - 1)v_{\rm esc}$ for the separation of outgoing and infalling mass shells for two different values of the compression ratio β (black curves) for model s11.2_3D.

Using the approximate formula of Timmes, Woosley & Weaver (1996) for the gravitational neutron star mass $M_{\rm grav}$,

$$M_{\rm grav} \approx M_{\rm by} - 0.075\,M_\odot \left(\frac{M_{\rm grav}}{M_\odot}\right)^2, \tag{4}$$

which provides a reasonable fit across different nuclear EoS, the estimated baryonic neutron star mass for s11.2_3D can be converted to a gravitational mass of $1.34\,M_\odot$, which would be well within the range of observed neutron star masses and slightly below the mean value of the higher mass population of neutron stars from iron core progenitors suggested by Schwab et al. (2010). For the 2D simulations, the estimated gravitational masses are higher by more than $0.1\,M_\odot$. The 3D effects responsible for the steeper rise of the explosion energy thus improve the agreement with the observational constraints considerably.

4 ASSESSMENT OF SHOCK REVIVAL IN THE 3D MODEL

In the remaining part of the paper, our main thrust will be to explain the physical mechanisms behind the pronounced differences between 2D and 3D simulations in the explosion phase presented in Section 3. We do not investigate the differences in the pre-explosion phase, because the numerical methodology used in this study only allows limited conclusions concerning the problem of shock revival in 3D for reasons detailed below. None the less, a few remarks about shock revival in model s11.2_3D are in order, if only to motivate why the remainder of this paper focuses completely on the explosion phase, and why simulations with a more rigorous treatment of the neutrino transport and the neutrino rates are needed to decide the fate of this particular progenitor model.

Superficially, our results for the $11.2\,M_\odot$ star in 3D may appear to be at odds with the recent core-collapse supernovae; simulations with multi-group neutrino transport that find either no shock revival at all in 3D or only delayed shock revival compared to 3D (Hanke et al. 2012; Hanke 2014; Tamborra et al. 2014b; Lentz et al. 2015; Melson et al. 2015a). Specifically, the $11.2\,M_\odot$ model failed

to explode in 3D (Tamborra et al. 2014b) in a simulation using the VERTEX-PROMETHEUS code (Rampp & Janka 2002; Buras et al. 2006a). However, one should not attach undue importance to the different outcomes of the VERTEX-PROMETHEUS and COCONUT-FMT models. Although reasonably close agreement with the more rigorous transport scheme in VERTEX can be reached with the FMT scheme, the differences noted by Müller & Janka (2015) are sufficiently large to matter for a marginal model like s11.2. The fact that we find an explosion merely underscores how close the $11.2\,M_\odot$ VERTEX model of Hanke (2014) and Tamborra et al. (2014b) comes to an explosive runaway, and that the extreme sensitivity of the supernova problem to the neutrino transport treatment and the microphysics (Lentz et al. 2012a,b; Melson et al. 2015a) requires highly accurate first-principle models in order to reliably decide whether an individual progenitor close to the explosion threshold explodes or fails (although 'imperfect' simulations may already unearth much of the relevant physics from such cases). Considering that the comparison between the FMT scheme and VERTEX revealed slightly better heating conditions for a $15\,M_\odot$ progenitor at early times, and that the average shock radius initially expands somewhat further in 3D than in 2D in the simulations of the $11.2\,M_\odot$ progenitor with VERTEX, the different outcome of the FMT and VERTEX runs is by no means unexpected.

Potentially, the emergence of large-scale bubbles aligned with the coordinate axis (Figs 4–6) also helps in pushing the 3D model above the explosion threshold at an early time (cp. Thompson 2000; Dolence et al. 2013; Fernández 2015 for the role of the bubble size in the development of runaway shock expansion). The alignment is clearly a consequence of our coordinate choice and may also be connected to the coarsening procedure for the polar region. Such artefacts are unavoidable for standard spherical polar, cylindrical, or Cartesian coordinates (where they manifest themselves as a preferred excitation of $m = 4$ modes instead), because the grid geometry and spacing dictate the effective numerical diffusivity and viscosity of a code, and physical instabilities will grow preferentially in directions where they are least suppressed (or even aided) by numerical dissipation. If there is sufficient time for instabilities like convection and the SASI to reach saturation and go through several overturn time-scales or oscillation periods, these initial artefacts from the growth phase are eventually washed out, but in a situation where the growth of certain modes accelerates rapidly (e.g. after the infall of the Si/SiO interface) and then freezes out, they can subsist throughout the simulation. None the less, we do not view this as a concern; the convective flow does not show any grid alignment prior to the infall of the interface, and outflows eventually develop in the equatorial plane as well. Moreover, we found no grid alignment of sloshing/spiral motions in SASI-dominated models (which will be reported elsewhere). In more realistic simulations, the explosion geometry will be dictated by anisotropies in the initial model, e.g. due to convective nuclear burning (Arnett 1994; Bazan & Arnett 1994, 1998; Asida & Arnett 2000; Kuhlen, Woosley & Glatzmaier 2003; Meakin & Arnett 2006, 2007a,b; Arnett & Meakin 2011; Couch & Ott 2015) or rotation. In a sense, the alignment of the most prominent high-entropy bubbles with the axis in model s11.2_3D is even fortunate for our further analysis because it eliminates the unavoidable grid alignment of 2D explosion models as a potential cause for the different energetics in 2D and 3D.

5 ANALYSIS OF 2D/3D DIFFERENCES

We now turn to the underlying physical mechanism responsible for the different evolution of the 2D and 3D models during the explosion phase. The first step towards understanding the different dynamics of the 2D and 3D models consists in considering the outflows and downflows separately [in the vein of Melson et al. (2015b)] to analyse the injection of mass and energy into the 'ejecta region' with positive binding energy [similar to Bruenn et al. (2014)]. We partition the computational domain into two regions with positive radial velocity ($v_r > 0$) and negative radial velocity ($v_r < 0$) and then compute total fluxes and averages of several hydrodynamic quantities. In order not to detract the reader from the physics, we work with Newtonian definitions here, and the generalization to the relativistic case is discussed in Appendix instead. Unless explicitly stated otherwise, the analysis is based on models s11.2_2Da and s11.2_3D, i.e. we always refer to model s11.2_2Da and not to model s11.2_2Db when talking about the 2D case.

5.1 Mass and enthalpy flux into the ejecta region

The first quantities to consider are the mass fluxes $\dot{M}_{\rm in}$ and $\dot{M}_{\rm out}$ in the downflows and outflows,

$$\dot{M}_{\rm in/out} = \int_{v_r \lessgtr 0} \rho v_r r^2 {\rm d}\Omega, \tag{5}$$

where ρ is the density, and the less- and greater-than signs refer to downflows and outflows, respectively. Furthermore, we define total enthalpy[4] and energy fluxes $F_{\rm h}$ and $F_{\rm e}$,

$$F_{\rm h,in/out} = \int_{v_r \lessgtr 0} \left[\rho(\epsilon + \boldsymbol{v}^2/2 + \Phi) + P\right] v_r r^2 {\rm d}\Omega \tag{6}$$

$$F_{\rm e,in/out} = \int_{v_r \lessgtr 0} \rho(\epsilon + \boldsymbol{v}^2/2 + \Phi) v_r r^2 {\rm d}\Omega, \tag{7}$$

where ϵ is the mass-specific internal energy, $\boldsymbol{v}$ is vectorial fluid velocity, and Φ is the Newtonian gravitational potential. The rationale for including the gravitational potential in these fluxes is that there is a conservation law for the total energy density $e_{\rm tot} = \epsilon + \boldsymbol{v}^2/2 + \Phi$,

$$\frac{\partial}{\partial t}\left[\rho\left(\epsilon + \frac{\boldsymbol{v}^2}{2} + \Phi\right)\right] + \nabla \cdot \left[\rho\left(\epsilon + \frac{\boldsymbol{v}^2}{2} + \Phi\right)\boldsymbol{v} + P\boldsymbol{v}\right] = 0, \tag{8}$$

if the gravitational potential is time independent and the conversion of rest-mass energy is either disregarded or nuclear rest masses are included in the internal energy. Since the diagnostic explosion energy is defined as an integral over the total energy of the ejecta, the energy budget of the ejecta naturally involves the total enthalpy flux from lower regions of the gain layer to the 'ejecta region' with $e_{\rm tot}$ if the boundary of the ejecta region remains at a roughly constant radius.

In Fig. 12, we show $\dot{M}_{\rm out}$ and the average total enthalpy and energy $\bar{h}_{\rm tot}$ and $\bar{e}_{\rm out}$ (defined as $\bar{h}_{\rm out} = F_{\rm h,out}/\dot{M}_{\rm out}$ and $\bar{e}_{\rm out} = F_{\rm e,out}/\dot{M}_{\rm out}$, and excluding rest-mass contributions) in the outflows at a radius of 400 km as a function of time. This radius has been chosen because recombination into α-particles, which roughly sets the final mass-specific total energy in the ejecta (Scheck et al. 2006), is already complete at this point, so that $F_{\rm h,\,out}$ roughly represents

[4] The quantity $h_{\rm tot} = \epsilon + P/\rho + \boldsymbol{v}^2/2 + \Phi$, which we shall usually designate in this paper as 'total enthalpy', is also referred to as Bernoulli integral or stagnation enthalpy in other contexts (including the case without gravity). In this paper, we prefer the term 'total enthalpy' to keep the terminology compact and stress its close relation to the total energy per unit mass.

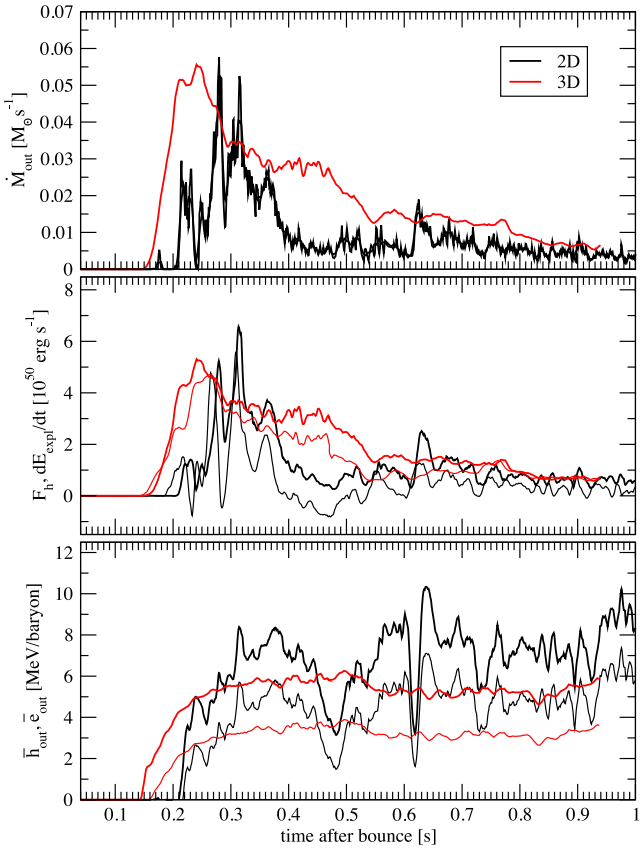

Figure 12. Comparison of key properties of the neutrino-driven outflows in 2D (black curves) and 3D (red curves) as measured at a radius of 400 km. The top panel shows the mass outflow rate $\dot{M}_{\rm out}$. The middle panel shows the total enthalpy flux $F_{\rm h,\,out}$ as defined in equation (6) (thick lines) alongside the time derivative $dE_{\rm expl}/dt$ of the explosion energy (thin lines). The average total enthalpy $\bar{h}_{\rm out}$ (thick lines) and total energy $\bar{e}_{\rm out}$ in the outflows are shown in the bottom panel.

the rate at which the net total energy is pumped into the ejecta region assuming steady-state conditions (i.e. small variations of $F_{\rm h,\,in}$ with time and radius). This is indeed a very good approximation as the comparison for $F_{\rm h,\,out}$ with the time derivative $dE_{\rm expl}/dt$ of the explosion energy as shown by the middle panel in Fig. 12. $dE_{\rm expl}/dt$ correlates extremely well with $F_{\rm h,\,out}$, but is slightly smaller. The difference is due to the accumulation of shocked material with slightly negative total energy and energy exchange with the downflows due to turbulent diffusion. The similarity of $dE_{\rm expl}/dt$ and $F_{\rm h,\,out}$ also indicates that explosive nuclear burning does not play a major role for the 11.2 $M_\odot$ model in agreement with earlier 2D simulations with the VERTEX-COCONUT code (Müller et al. 2012a).

On average, the total enthalpy flux into the ejecta region is larger in 3D than in 2D as expected from the different evolution of the explosion energy. Interestingly, the relative difference between 2D and 3D in the mass outflow rate $\dot{M}_{\rm out}$ is even larger than for $F_{\rm h,\,out}$. The smaller outflow rate in 2D is partially compensated by a larger average mass-specific total enthalpy and energy in the outflows, which can be *larger* than the recombination energy (7–8.8 MeV/nucleon). Thus, care must be exercised in explaining differences between 2D and 3D based on the mass outflow rate or the total mass in the gain region alone (Scheck et al. 2006; Melson et al. 2015b) assuming the same contribution to the explosion energy per unit mass from nucleon recombination into α-particles and heavy nuclei irrespective of the dimensionality. That assumption would require similar average enthalpies and energies in the outflows in 2D and 3D, which is clearly not the case in general; the differences can be as large as several MeV/nucleon. Recombination still sets the scale for the asymptotic total energy per unit mass of neutrino-heated ejecta, but hydrodynamic effects modify its precise value in 2D and 3D in different directions as we shall explain below.

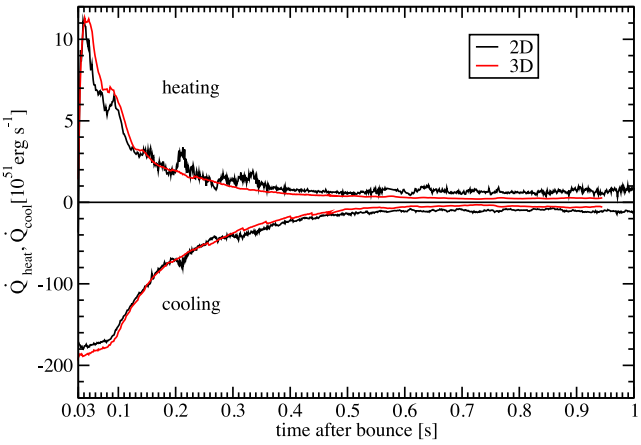

Figure 13. Volume-integrated heating/cooling rates $\dot{Q}_{\rm heat}$ and $\dot{Q}_{\rm cool}$ in the gain and cooling region for models s11.2_2Da and s11.2_3D. The inner boundary of the cooling region is defined (somewhat arbitrarily) by a density of 10^{13} g cm^{-3}. Note that a different scale is used for both rates.

These differences are all the more astonishing because the volume-integrated neutrino heating rate $\dot{Q}_{\rm heat}$ in the gain region (Fig. 13) is very similar in 2D and 3D. Especially at late times, $\dot{Q}_{\rm heat}$ is consistently *higher in 2D* than in 3D (as is the time-integrated neutrino energy deposition). Assuming that the outflow rate is determined by the total heating rate and the binding energy $e_{\rm gain}$ at the gain radius as $\dot{M}_{\rm out} \sim \dot{Q}_{\rm heat}/|e_{\rm gain}|$, the lower outflow rate in 2D suggests that the material at the gain radius is more strongly bound in this case. This is borne out by Fig. 14, which shows that the binding energy at the gain radius is larger in 2D by up to a factor of ∼2 at late times. This is partly due a stronger recession of the gain radius $r_{\rm gain}$ (bottom panel of Fig. 14) as a result of which the typical energy scale $GM/r_{\rm gain}$ (M being the neutron star mass) at the gain radius is larger. However, it is evident that this effect cannot fully account for the difference in $e_{\rm gain}$. The small value of $e_{\rm gain}$ in 3D indicates that it is not determined by the gravitational energy scale alone. Indeed, a much better estimate for the scale of $e_{\rm gain}$ can be obtained if we suppose that the Bernoulli integral (including rest masses) at the gain radius is roughly zero,

$$\epsilon + \frac{\boldsymbol{v}^2}{2} + \frac{P}{\rho} + \Phi = 0. \tag{9}$$

If we split the internal energy ϵ into a thermal component $\epsilon_{\rm therm}$ and a rest-mass contribution $\epsilon_{\rm rm}$ (normalized to ^{56}Fe), and assume vanishing velocities as well as an ideal gas equation $P = \epsilon_{\rm therm}/3$ of state for photons and non-degenerate relativistic electrons and positrons, this leads to

$$\epsilon_{\rm therm} + \epsilon_{\rm rm} + \frac{P}{\rho} - \frac{GM}{r_{\rm gain}} = 0, \tag{10}$$

$$\frac{4}{3}\epsilon_{\rm therm} + \epsilon_{\rm rm} - \frac{GM}{r_{\rm gain}} = 0, \tag{11}$$

$$\epsilon_{\rm therm} = \frac{3}{4}\left(\frac{GM}{r_{\rm gain}} - \epsilon_{\rm rm}\right), \tag{12}$$

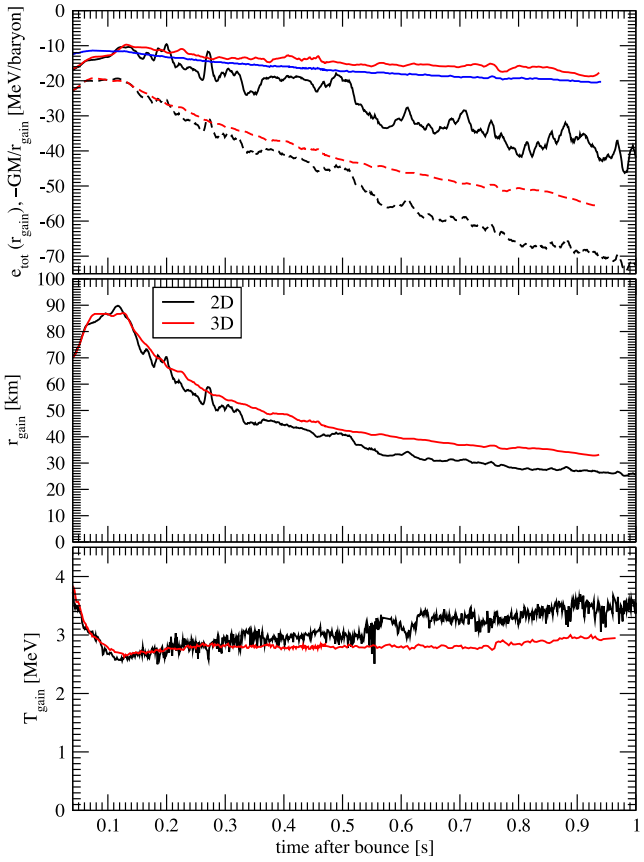

Figure 14. Properties of the gain radius in 2D and 3D. The top panel shows the binding energy (i.e. the sum of the gravitational, kinetic, and internal energy) at the gain radius in 2D (black solid curve) and 3D (red solid curve) alongside the Newtonian potential of the neutron star $GM/r_{\rm gain}$ (dashed lines), which sets the typical energy scale at the gain radius. Here, M is the neutron star mass and $r_{\rm gain}$ is the gain radius. The estimate for $e_{\rm gain}$ from equation (13), which is based on the assumption that the Bernoulli integral at the gain radius is zero, is shown in blue for comparison. The middle panel shows $r_{\rm gain}$ itself, and the bottom panel shows the angle-averaged temperature at the gain radius, $T_{\rm gain}$.

where M is the neutron star mass. For an electron fraction of $Y_{\rm e} = 0.5$, $\epsilon_{\rm rm}$ would be identical to the recombination energy of $\epsilon_{\rm rec} \approx 8.8\,{\rm MeV/nucleon}$ from protons and neutrons with equal mass fractions into iron group elements, and for our purposes this still provides a sufficient approximation even though we have $Y_{\rm e} < 0.5$ at the gain radius. For the binding energy $e_{\rm gain}$ (in which we excluded rest masses), we thus obtain

$$e_{\rm gain} \approx \epsilon_{\rm therm} - \frac{GM}{r_{\rm gain}} \approx -\frac{3}{4}\epsilon_{\rm rec} - \frac{GM}{4r_{\rm gain}}. \qquad (13)$$

As shown in Fig. 14, this still overestimates $|e_{\rm gain}|$ a bit, but accounts for the slow rise of $|e_{\rm gain}|$ compared to the gravitational energy scale $GM/r_{\rm gain}$ during the contraction of the neutron star.

While the different absolute value of the binding energy at the gain radius is part of the explanation for the different mass outflow rates, there is also an additional effect at play. In general, the mass outflow rate will only be approximately given by $\dot{M}_{\rm out} \sim \dot{Q}_{\rm heat}/|e_{\rm gain}|$, and one can introduce an efficiency parameter $\eta_{\rm out}$ to compare the actual mass outflow rate with this fiducial rate,

$$\eta_{\rm out} = \frac{|e_{\rm gain}|\dot{M}_{\rm out}}{\dot{Q}_{\rm heat}}. \qquad (14)$$

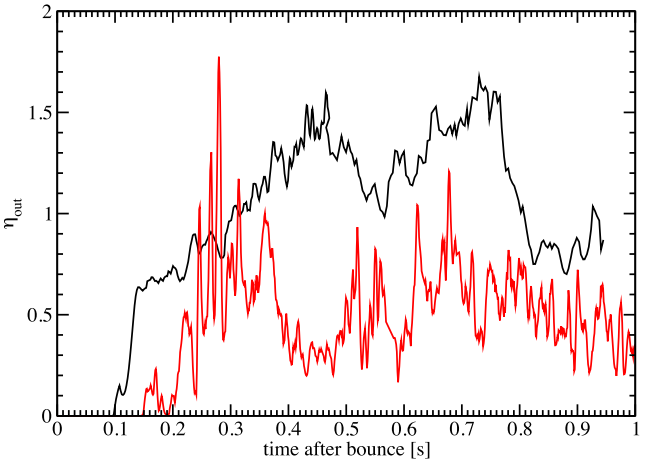

Figure 15. Outflow efficiency $\eta_{\rm out}$, for models s11.2_2Da and s11.2_3D. $\eta_{\rm out}$ is defined as the ratio between the actual mass outflow rate $\dot{M}_{\rm out}$ and a fiducial scale $\dot{Q}_{\rm heat}/|e_{\rm gain}|$ for the mass-loss rate, see equation (14). Note that $\eta_{\rm out}$ is not limited to values $\eta_{\rm out} \leq 1$ because fresh matter for the neutrino-heated outflows is also supplied by lateral mixing with the downflows above the gain radius (where the matter is less tightly bound than at the gain radius) and because recombination also partly contributes in lifting the material out of the gravitational potential well.

$\eta_{\rm out}$ is plotted in Fig. 15. On average, the outflow efficiency $\eta_{\rm out}$ is also considerably larger in 3D (where it fluctuates around $\eta_{\rm out} \approx 1$) than in 2D ($\eta_{\rm out} \approx 0.5$).

Our analysis of the outflows has thus revealed two reasons for lower explosion energies in 2D. The mass-loss rate (and hence the energy flux into the ejecta region) is lower because the ejected material is initially bound more tightly at the gain radius before being lifted out of the gravitational potential well, and for a given binding energy $e_{\rm gain}$ at the gain radius, the conversion of neutrino heating into an outflow is less efficient.

5.2 Causes for weak explosions in 2D

These two effects, as well as the higher asymptotic energy per unit mass in 2D, can be traced to the constrained axisymmetric flow geometry and a fundamentally different behaviour of the accretion downflows in 2D compared to 3D. The different flow morphology is illustrated qualitatively in Fig. 16, which shows snapshots (for different spatial scales) of the radial velocity and entropy in 2D and 3D for a representative post-bounce time of 400 ms.

5.2.1 Morphology and dynamics of outflows and accretion downflows in 2D and 3D

These snapshots reveal that the interface between the outflows and the colder, low-entropy material becomes turbulent due to the Kelvin–Helmholtz instability in 3D, which distorts the downflows as they approach the proto-neutron star (as already mentioned in Section 3), whereas Kelvin–Helmholtz instabilities are noticeably absent at the shear interfaces between the broad equatorial downflow and the polar bubbles in 2D (middle and bottom row in Fig. 16). The tendency of the downflows to become more turbulent in 3D has been recognized already by Melson et al. (2015b) in their $9.6\,{\rm M}_\odot$ model, although the morphological difference between 2D and 3D is much more pronounced in a continuously accreting model like the $11.2\,{\rm M}_\odot$ progenitor. Moreover, although there may be a deeper connection between the two phenomena, the stability of the shear

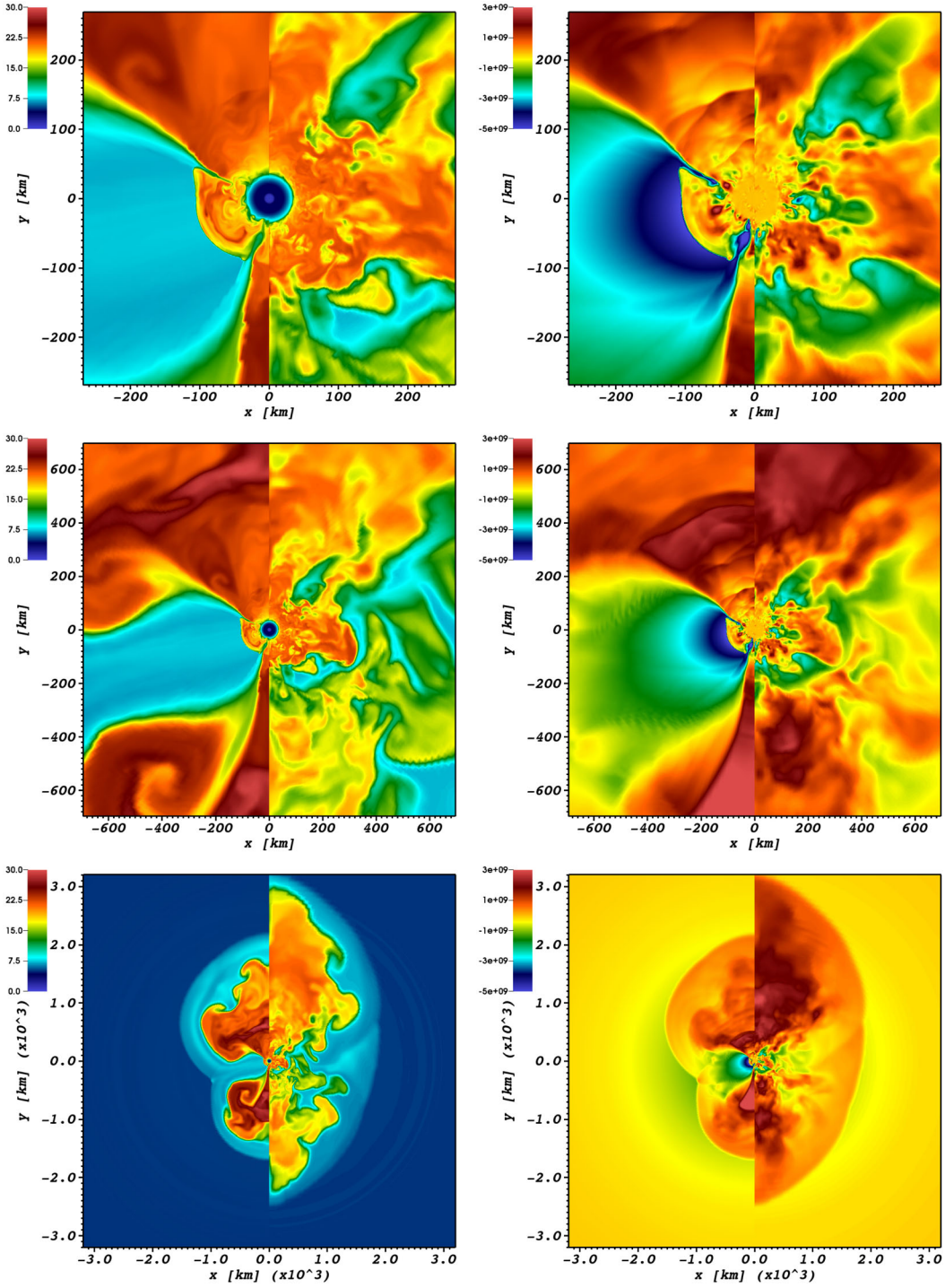

Figure 16. Snapshots of the specific entropy s (left column, measured in k_b/nucleon) and the radial velocity v_r (right column, measured in cm s^{-1}) for model s11.2_2Da (left halves of the individual panels) and for a slice of model s11.2_3D (right halves) at a post-bounce time of 400 ms. The same data are shown in all plots, only the zoom level is different. Note the broad equatorial accretion downflow and the formation of a secondary accretion shock at a radius of ∼100 km in 2D.

interfaces in 2D is likely due to a different reason than the emergence of large-scale structures in the pre-explosion phase (Hanke et al. 2012) that has been explained by the inverse turbulent energy cascade in 2D (Kraichnan 1967). Despite the inverse turbulent cascade, subsonic shear layers/interfaces remain prone to the Kelvin–Helmholtz instability in 2D, and 2D supernova simulations are easily able to resolve the instability (Müller et al. 2012b; Fernández 2015) even without extraordinary high resolution.

The situation changes, however, for the supersonic shear interfaces between the downflows and the neutrino-heated bubbles that we encounter during the explosion phase. Here, the classical growth rate $\omega = k\Delta u/2$ (where k is the wavevector and Δu is the transverse

velocity jump across the interface) in the vortex sheet approximation for incompressible flow is no longer applicable. Instead, modes with a sufficiently high effective Mach number $\mathrm{Ma} = \Delta u \cos\theta / c_\mathrm{s}$ (where c_s is the sound speed and θ is the angle between the wavevector and the vectorial velocity jump) are stabilized (Gerwin 1968), although the stability analysis is more complicated if finite-width shear layers are considered (Blumen 1970; Blumen, Drazin & Billings 1975; Drazin & Davey 1977; Choudhury & Lovelace 1984; Balsa & Goldstein 1990).[5] This implies that the Kelvin–Helmholtz instability can be partially or completely suppressed in 2D (where $\cos\theta = 1$), while there are always unstable modes in 3D since $\cos\theta$ can be arbitrarily small.[6] In principle, it is conceivable that numerical diffusivity and viscosity further help to suppress the Kelvin–Helmholtz instability more strongly and earlier than the physics might dictate, but the fact that the instability evidently operates in the 3D model provides evidence that the numerical resolution cannot be faulted for the behaviour of the 2D models. Furthermore, the stability of the accretion downflows is a persistent feature even in high-resolution 2D models with continuing accretion (Bruenn et al. 2014); it is thus without doubt physical in origin.

The 'turbulent braking' of the downflows in 3D is reflected quantitatively in radial profiles of the average velocity $\bar{v}_\mathrm{in/out}$, entropy $\bar{s}_\mathrm{in/out}$, and mass-specific total energy $\bar{e}_\mathrm{tot,rm,in/out}$ of the downflows and outflows. We define these quantities as density-weighted averages (denoted by bars) of the radial velocity v_r, the specific entropy s, and the total energy e_tot as

$$\bar{v}_\mathrm{in/out} = \frac{\int_{v_\mathrm{r}\lessgtr 0} \rho v_\mathrm{r}\,\mathrm{d}\Omega}{\int_{v_\mathrm{r}\lessgtr 0} \rho\,\mathrm{d}\Omega} \tag{15}$$

$$\bar{s}_\mathrm{in/out} = \frac{\int_{v_\mathrm{r}\lessgtr 0} \rho s\,\mathrm{d}\Omega}{\int_{v_\mathrm{r}\lessgtr 0} \rho\,\mathrm{d}\Omega} \tag{16}$$

$$\bar{e}_\mathrm{tot,in/out} = \frac{\int_{v_\mathrm{r}\lessgtr 0} \rho e_\mathrm{tot,rm}\,\mathrm{d}\Omega}{\int_{v_\mathrm{r}\lessgtr 0} \rho\,\mathrm{d}\Omega}, \tag{17}$$

and show the results for models s11.2_2Da and s11.2_3D at a post-bounce time of 400 ms in Fig. 17. Moreover, we consider radial profiles of the mass and total enthalpy fluxes $\dot{M}_\mathrm{in/out}$ and $\dot{F}_\mathrm{h,rm,in/out}$ in both streams in Fig. 18; these are computed according to equations (5) and (6). However, for computing radial profiles we include rest-mass contributions in the total energy and the total enthalpy flux (as denoted by the additional subscript 'rm'). This

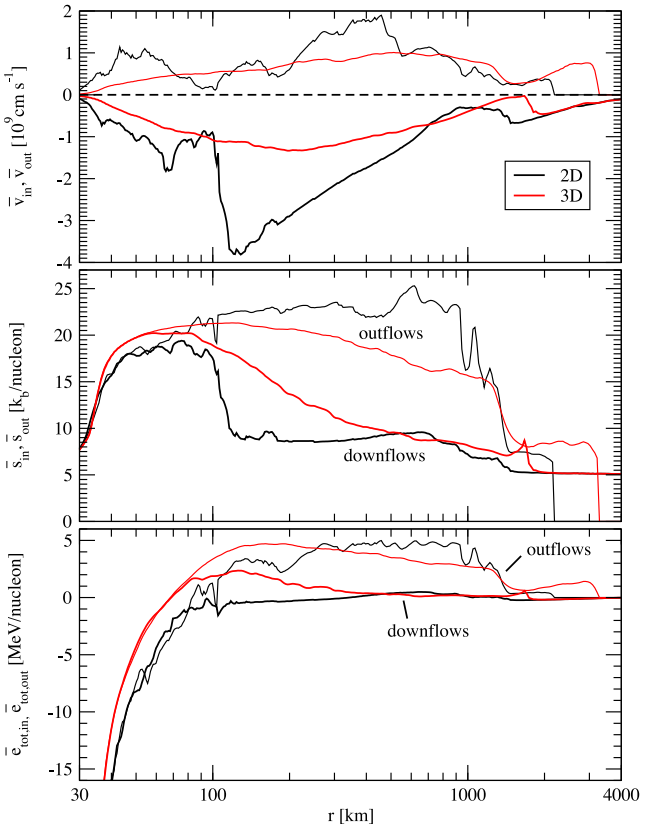

Figure 17. Radial profiles of the average velocity (top panel), entropy (middle panel), and total energy (bottom) per nucleon in the outflows (thin lines) and downflows (thick lines) in 2D (black) and 3D (red) at a post-bounce time of 400 ms. Note that rest-mass contributions are included in the total energy here.

definition has the advantage that both $\dot{M}_\mathrm{in,out}$ and $\dot{F}_\mathrm{h,rm,in/out}$ are constant in the limit of stationary streams without mass, energy, and momentum exchange, so that changes in these fluxes serve as useful indicators for lateral mixing between the outflows and downflows.

Due to turbulent braking (i.e. by an effective turbulent eddy viscosity), the average infall velocity in the downflows reaches only 1.4×10^9 cm s^{-1} in 3D, and decreases in magnitude once the downflows penetrate further down than a radius of ∼200 km. By contrast, the downflows reach a sizeable fraction of the free-fall velocity in 2D before they are abruptly decelerated at a secondary accretion shock at $r \approx 100$ km. However, the outflow velocities are also higher in 2D.

During the phase considered here, the entropy of the downflows does not vary considerably in 2D between $r \approx 100$ and $r \approx 1000$ km (where the equatorial downflow forms from two converging lateral flows). Similarly, the 'flux-averaged enthalpy' $F_\mathrm{h,rm,in/out}/\dot{M}_\mathrm{in/out}$ (bottom panel of Fig. 18) does not change appreciably in this region. This is a further indication for a lack of dissipation by turbulent eddy viscosity and of lateral mixing between the downflows and outflows. By contrast, the slope in $\bar{s}_\mathrm{in}$ and $\bar{s}_\mathrm{out}$ and the 'flux-averaged' total enthalpy $F_\mathrm{h,rm,in/out}/\dot{M}_\mathrm{in/out}$ point to lateral mixing between the downflows and outflows in 3D. The increase of $F_\mathrm{h,rm,in/out}/\dot{M}_\mathrm{in/out}$ in the downflows during the infall from the shock is mirrored by a decrease of $F_\mathrm{h,rm,in/out}/\dot{M}_\mathrm{in/out}$ with radius in the outflows due to turbulent mixing of the hot ejecta with colder matter from the downflows. This explains why the neutrino-heated ejecta

[5] It is noteworthy that laser-driven plasma experiments may be able to capture this effect and quantify the reduced growth or suppression of the Kelvin–Helmholtz instability in 2D (Malamud et al. 2013).

[6] Loosely speaking, a small value of $\cos\theta$ guarantees that sound waves on either side of the vortex sheet can propagate in both directions along the wavevector $\boldsymbol{k}$ of a given perturbation mode to mediate the pressure feedback required for the growth of the Kelvin–Helmholtz instability. For a given vectorial velocity $\pm\boldsymbol{u}/2$ of the fluid on either side of the interface, the sound waves with direction $\boldsymbol{n}$ and velocity c_s in either of the fluids will have a velocity component $(\pm\boldsymbol{u}/2 + \boldsymbol{n}c_\mathrm{s}) \cdot \boldsymbol{k}/|\boldsymbol{k}| = \pm u/2 \cos\theta + c_\mathrm{s}\boldsymbol{n} \cdot \boldsymbol{k}/|\boldsymbol{k}|$ along the direction of $\boldsymbol{k}$ in the rest frame. If $\cos\theta$ is sufficiently small, this velocity component can take on either sign depending on $\boldsymbol{n}$ in both fluids. In 2D, we always have $\pm\boldsymbol{u}/2 \cdot \boldsymbol{k}/|\boldsymbol{k}| = u/2$, and sound waves cannot propagate in both directions any longer for sufficiently large u. Note that this is only a heuristic explanation that cannot predict the critical Mach number correctly; section B in Gerwin (1968) and the other aforementioned references should be consulted for a rigorous derivation of the dispersion relation.

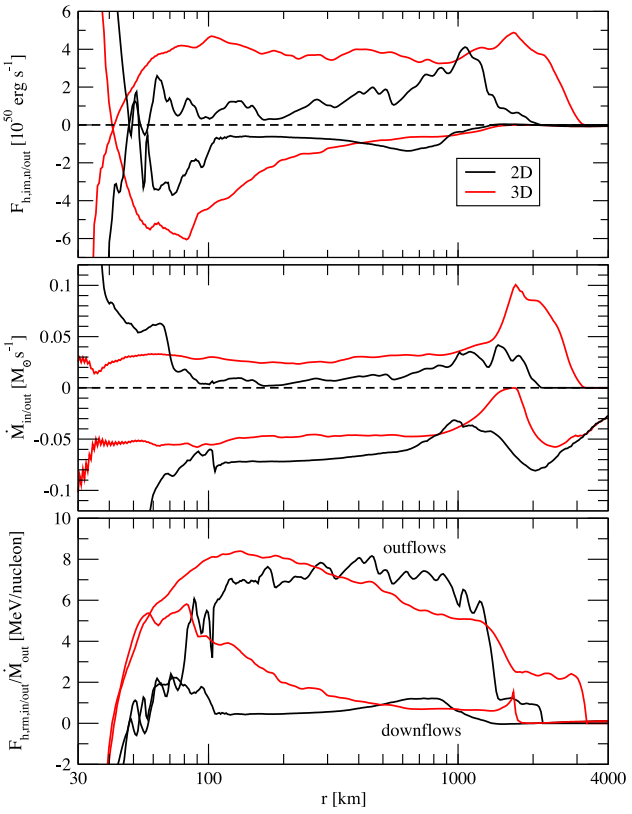

Figure 18. Overview of the mass and energy fluxes in the outflows and downflows in 2D. The top panel shows the total enthalpy fluxes $F_{\rm h,\,rm,\,in/out}$ in the outflows (positive values) and downflows (negative values) in 2D (black) and 3D (red) at a post-bounce time of 400 ms. The middle panel shows the mass inflow/outflow rates $\dot{M}_{\rm in/out}$, and the bottom panel shows the average flux-weighted total enthalpies $F_{\rm h,rm,in/out}/\dot{M}_{\rm in/out}$. Note that rest-mass contributions are included in the total entropy here, unlike in Figs 12 and 17.

contribute only ∼5−6 MeV/nucleon to the diagnostic explosion energy, instead of the 7–8.8 MeV/nucleon available from nucleon recombination.

There is thus ample evidence that turbulent viscosity and diffusion brake the accretion funnels and transfer energy from the outflows. It is tempting to invoke this as an explanation for the lower binding energy at the gain radius in 3D (Fig. 14). At first glance, the fact that *both* the downflows and outflows are less strongly bound in 3D at the bottom of the gain layer (bottom panel of Fig. 17) may seem to conflict with this assumptions, but the lower binding energies of the outflows at small radii are to be expected because the supply for outflow comes from freshly accreted matter that has undergone turbulent braking in the downflows. Turbulent braking and turbulent diffusion are perfectly acceptable explanations for *internal* energy distribution within the gain region (but not the higher enthalpy flux into the ejecta region, see below), and may thus account for the lower $|e_{\rm gain}|$ in 3D and hence for the higher mass outflow rates.

Moreover, the turbulent braking in 3D may have implications for the final neutron star masses. In Section 3.3, we assumed that the 'mass cut' occurs roughly when the shock accelerates the newly swept-up material to the escape velocity. Without efficient lateral momentum transfer and without pressure support from an expanding hot bubble from below, it seems inevitable that material over existing downflows must eventually fall on to the neutron star if this condition is not met. Since the free-fall time-scale at radii of several thousands of kilometres (where the initial mass cut estimated in Section 3.3 is located) is of the order of seconds, accretion must necessarily last over a correspondingly long duration. On the other hand, if the downflows are braked by a turbulent eddy viscosity below a certain radius in 3D, slowly moving matter in the downflows may instead be entrained by the high-entropy bubbles in regions where the angular-averaged velocity is already positive, so that the residual accretion on to the neutron star may cease earlier and the total mass accreted during the

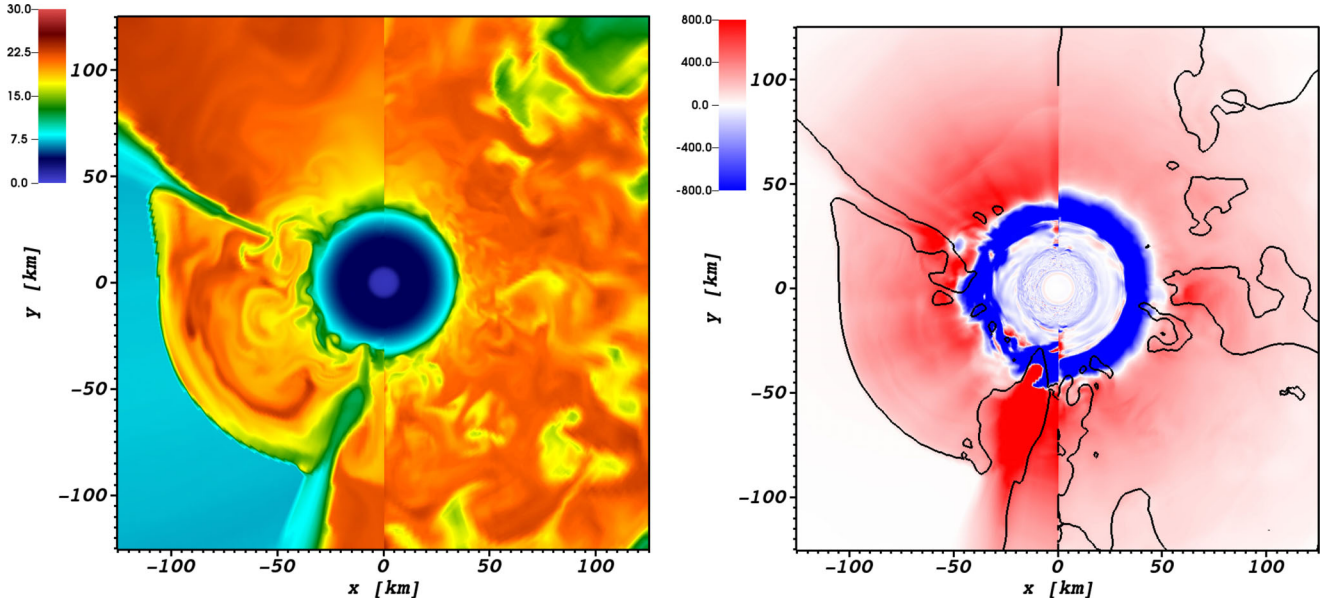

Figure 19. Left: entropy s in $k_{\rm b}$/nucleon in the vicinity of the proto-neutron star in 2D (left half of panel) and 3D (right half of panel) at a post-bounce time of 400 ms (identical to Fig. 16 except for the zoom level). Right: heating/cooling rate in MeV/nucleon in 2D (left half of panel) and 3D (right half of panel). Isovelocity contours for a radial velocity of $v_{\rm r} = -10^9\,{\rm cm\,s^{-1}}$ are shown to indicate the location of the accretion downflows. Note that much of the neutrino heating occurs in the downflows and the confined high-entropy bubble in the equatorial region and hence does not drive an outflow.

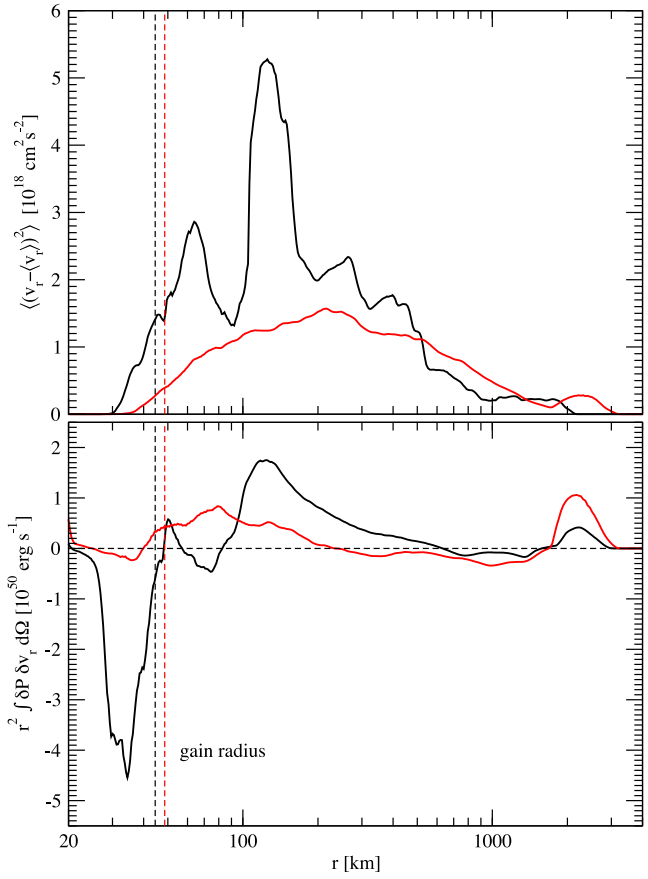

Figure 20. Top: radial velocity dispersion $\langle (v_r - \langle v_r \rangle)^2 \rangle$ in 2D and 3D at a post-bounce time of 400 ms. Bottom: radial profiles of the 'acoustic' energy flux $r^2 \int \delta P\, \delta v_r\, d\Omega$ in 2D and 3D at a post-bounce time of 400 ms. The curves show temporal averages over several time steps.

explosion phase may be considerably lower than that estimated in Section 3.3. Longer 3D simulations will be necessary to investigate this hypothesis.

However, the internal redistribution of energy within the gain region in 3D *cannot* account for the significantly higher total enthalpy flux in the outflows and the faster rise of the explosion energy. The higher outflow rate will come at the expense of energy loss from the outflows to the downflows – the overall conservation law cannot be cheated. Consequently, there must be additional mechanisms that remove energy from the gain region in 2D and reduce the outflow efficiency $\eta_{\rm out}$ (Fig. 15) compared to 3D. The different dynamics of the outflows and downflows none the less remains a crucial element of the explanation because it provides the basis for three mechanisms discussed in the subsequent sections.

5.2.2 *Energy loss by wave excitation*

The lack of turbulent braking in 2D implies that the accretion funnels either hit the neutron star directly with a high impact velocity or are decelerated abruptly in a secondary accretion shock (top row of Fig. 16). Even in the latter case, thin accretion funnels still penetrate the hot, neutrino-heated matter all the way down to the gain radius, cutting off a confined high-entropy bubble from the outflows. In the snapshots shown in Figs 16 and 19 (with an even higher zoom level), these narrow downflows strike the proto-neutron star surface with velocities of up to 6×10^9 cm s^{-1}. As a result, they overshoot considerably into the convectively stable cooling layer and excite strong wave activity. The emission of strong acoustic waves that steepen into shocks and then dissipate is immediately evident from the top-right panel of Fig. 16, but the deceleration of the downflows also excites strong g modes in the neutron star surface region (a phenomenon that has been thoroughly analysed in the context of gravitational wave emission; cp. Marek, Janka & Müller 2009; Murphy, Ott & Burrows 2009; Müller, Janka & Marek 2013). In 3D, overshooting is much less pronounced, and so is the excitation of acoustic waves and g modes. This can be seen from the conspicuous absence of sawtooth-like features in the velocity and by considering the radial velocity dispersion $\langle (v_r - \langle v_r \rangle)^2 \rangle$, which is significantly smaller in 3D below the gain radius (top panel of Fig. 20). This result is in agreement with other 3D simulations of supernova explosions using self-consistent neutrino transport (Melson et al. 2015b) and parametrized neutrino heating (Murphy et al. 2013; Handy et al. 2014) and linear theory, which suggests that the excitation of waves (g modes in particular) at convective boundaries is strongly sensitive to the convective Mach number Ma and becomes very efficient for Ma $\sim$ 1 (Goldreich & Kumar 1990; Lecoanet & Quataert 2013).

What has been missed so far, however, is that the excitation of g modes constitutes a *non-advective energy drain* in 2D; it transports energy from the lower layers of the gain regions deep into the cooling region *without* the need to transport mass. If the g-mode energy flux is sufficiently high, it provides a very likely explanation for the permanently higher binding energy at the gain radius in 2D. Unfortunately, the g-mode energy flux in our simulations cannot readily be quantified; this would not only require performing a full spherical Reynolds decomposition, but also detailed knowledge about the dispersion relation of the g modes, which is beyond the scope of this paper. However, since the transfer of the kinetic energy from the downflows into g modes involves $P\,dV$-work on to the neutron star surface and any turbulent energy flux into deeper layers should show up in correlated pressure and velocity fluctuations in a transition layer between the convective gain region and the convectively stabilized cooling layer, we can formulate a crude estimate for the g-mode flux by computing what is nominally an acoustic luminosity, namely

$$L_{P\,dV} = r^2 \int \delta P\, \delta v_r\, d\Omega, \tag{18}$$

where δP and δv_r denote the deviations of the pressure and radial velocity from their respective angular averages. The resulting estimates for the flux are shown in the bottom panel of Fig. 20 and point to a sizeable energy flux of the order of several 10^{50} erg s^{-1} from the vicinity of the gain radius into the deeper layers of the proto-neutron star surface (carried by g modes) and to the outer regions of the gain layer (carried by acoustic waves). Such large fluxes are comparable to the typical total enthalpy flux in the outflows and even to the volume-integrated neutrino heating rate, and therefore need to be accounted for in the total energy budget of the gain region.

Incidentally, the excitation of acoustic waves also provides an explanation for the high entropy (Fig. 17) and total enthalpy (Figs 12 and 18) in the outflows in 2D, which can still increase somewhat at radii where neutrino heating is essentially irrelevant. The dissipation of the acoustic waves in the expanding hot bubble helps to increase the total energy and entropy in the ejecta region beyond the $\sim$7–8.8 MeV available from nucleon recombination, but since these waves carry only part of the energy lost by the

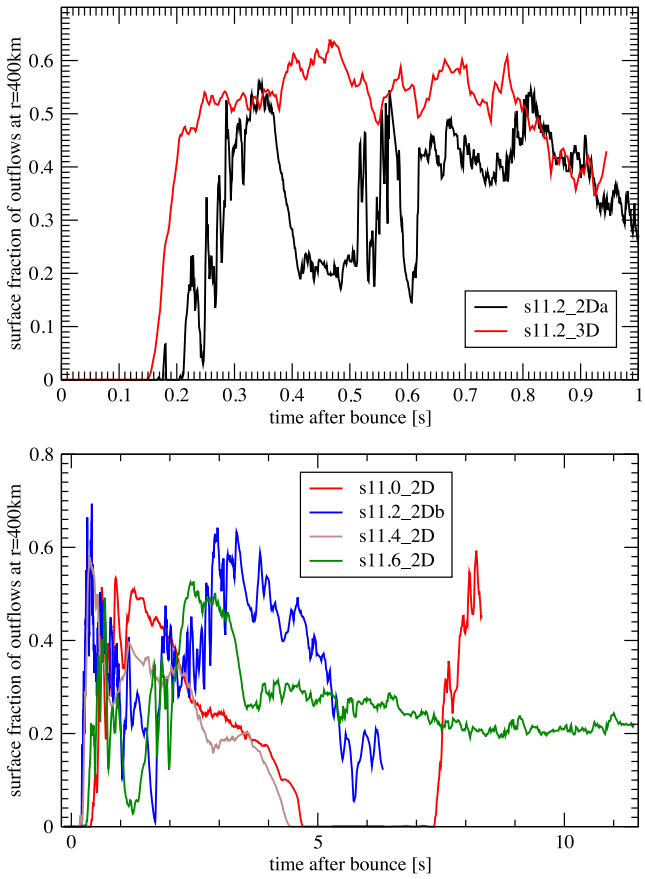

Figure 21. Top: surface fraction occupied by the outflows in models s11.2_2Da (black) and s11.2_3D (red) at a radius of 400 km. The surface fraction is relatively stable with some fluctuations around 0.5 in 3D. In 2D, it reaches similar values while the outflows are stable, but occasionally drops to significantly smaller values as a result of outflow constriction. Bottom: long-time evolution of the outflow surface fraction for the 2D models s11.0_2D, s11.2b_2D, s11.4_2D, and s11.6_2D.

downflows due to their interaction with the convective boundary, this effect cannot compensate for the lower mass outflow rate in 2D, and the net effect of wave excitation in 2D remains a detrimental one.

The importance of wave excitation at the convective boundary will inevitably vary between different 2D models depending on the explosion geometry and the duration of accretion. If neutrino heating is strong, the explosion energy rises steeply, and shock expansion is fast as in the models of Bruenn et al. (2013, 2014), it may play a less prominent role. The formation of secondary accretion shocks as in our 2D models is likely to increase the energy loss by wave excitation tremendously because the efficiency of this process also depends on the frequency overlap between the convective forcing and the excited modes (Goldreich & Kumar 1990; Lecoanet & Quataert 2013). The formation of a secondary accretion shock provides for fluctuations with typical frequencies inversely proportional to the short sound-crossing time-scale (of the order of milliseconds) in the confined bubble. Furthermore, the stochastic forcing of g modes in 2D by one or two strong downflows is presumably also more efficient than in 3D, where there are more smaller and uncorrelated downflows.

Finally, we comment on similarities and differences between g mode and acoustic wave excitation between our models and the acoustically driven explosion models of Burrows et al. (2006, 2007), where a strong flux acoustic wave, excited by an $\ell = 1$ *core* g mode with amplitudes of several kilometres, is responsible for shock expansion in the first place. Our 2D models are similar to those of Burrows et al. (2006, 2007) only in the sense that energy deposition by acoustic waves contributes to the growth of the explosion energy, but different from their simulations the acoustic contribution remains subdominant compared to the volume-integrated neutrino heating rate, which is more than four times larger at the time shown in Fig. 20 [a constellation that Burrows et al. (2007) anticipated when postulating a 'hybrid mechanism' with combined heating by neutrinos and acoustic waves]. Moreover, the excitation mechanism for acoustic waves is genuinely different in our case; they are excited *directly* by the interaction of the downflows with the convectively stable neutron star surface layer without the need to channel the accretion power through an $\ell = 1$ core g mode as a 'transducer' as in the models of Burrows et al. (2006, 2007). Such a large-amplitude core g mode is not found in our simulations (and could not have arisen simply because of the spherically symmetric treatment of the neutron star core), and the outer g modes of rather modest amplitude excited in our models could not act as an efficient transducer in the vein of Burrows et al. (2006, 2007) due to neutrino losses (see below). It is interesting to note that direct excitation at the convective boundary still allows acoustic waves to contribute (albeit at a minor level) to the explosion energy in 2D even without such a transducer.

Acoustic energy deposition also remains a secondary effect in so far as this direct excitation mechanism works efficiently only *after* the onset of the explosion once the typical Mach number of the downflows is sufficiently high. Moreover, contrary to Burrows et al. (2006, 2007) the net effect of wave excitation in our models is still harmful because the power pumped into *outer* g modes constitutes an energy drain that outweighs the rate of energy deposition by acoustic waves by far. Different from their models where the energy in the core g mode is eventually 'recycled' into an acoustic energy flux that drives shock expansion, the energy pumped into the outer g mode is manifestly lost due to neutrino cooling in our case, and the mode coupling analysis of Weinberg & Quataert (2008) suggests that this should also happen if the core g mode is excited due to non-linear mode coupling.

5.2.3 *Steric hindrances*

In addition to energy loss by wave excitation, which contributes to the higher binding energy at the gain radius, the growth of the explosion energy in 2D is further hampered by the fact that much of the neutrino energy deposition occurs in regions where the heated matter cannot directly escape in an outflow, i.e. either directly in the accretion funnels or in high-entropy bubbles confined by downflows and a secondary accretion shock like the equatorial bubble in Figs 16 and 19, a phenomenon for which we borrow the term 'steric hindrance' from chemistry. In principle, such bubbles could eventually push the secondary accretion shock out by undergoing 'secondary shock revival', but as long as the amount of heating is insufficient, the bubble cannot break through the surrounding and overlying downflows.

In the snapshot shown in the right-hand panel of Fig. 19, the surface fraction covered by the confined bubble and the downflows exceeds 50 per cent, and the heating rate per unit mass is also largest in the downflows. Since the fast downflows generally occupy a surface fraction of $\gtrsim$50 per cent in 2D outside the typical location of a

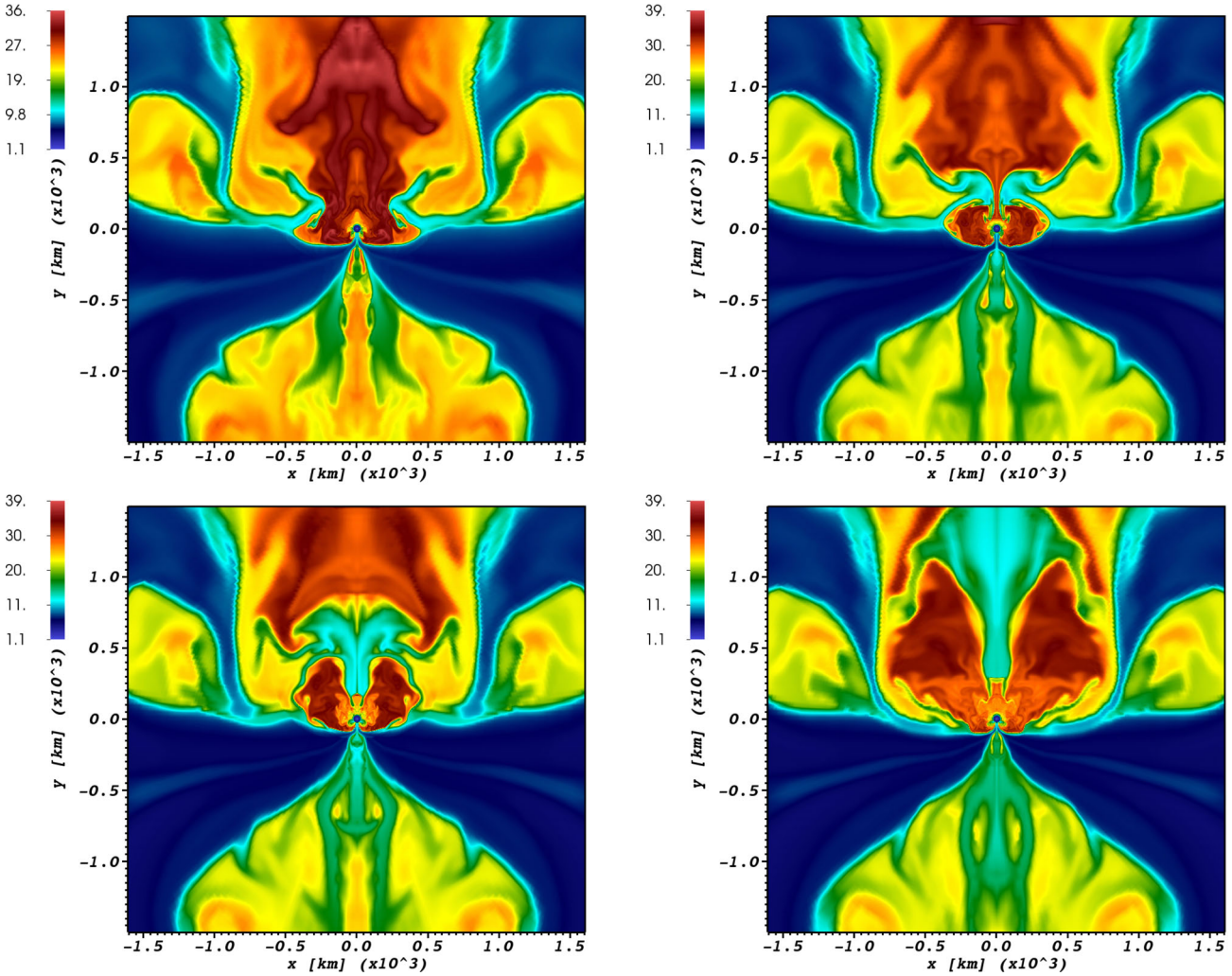

Figure 22. Constriction and partial shredding of an outflow in model s11.2_2Da, shown by snapshots of the entropy at post-bounce times of 592, 611, 628, and 655 ms. A downflow (cyan) originating from a Rayleigh–Taylor plume of cold matter penetrates the hot neutrino-heated bubble in the northern hemispheres (top left), constricts the neutrino-heated bubble to a tenuous outflow as it approaches the axis (top right), and eventually a considerable amount of cold material is mixed into the outflow (bottom left). While the ejection of matter continues (bottom right), the mixing event lowers the average total energy per unit mass in the ejecta.

secondary shock at $\lesssim$100 km (see Fig. 21), roughly half of the neutrino heating is not used to power outflows in 2D, and consequently the outflow efficiency oscillates around $\eta_{\rm out} \sim 0.5$ with some excursions to higher values during the early explosion phase (Fig. 15). By contrast, the neutrino-heated material can escape unhindered in any direction in 3D apart from some limited turbulent energy and momentum loss to the downflows, and the resulting outflow efficiency is of the order of $\eta_{\rm out} \sim 1$.

5.2.4 *Constriction of outflows and vertical mixing*

Finally, the outflows in axisymmetric 2D simulations are less 'stable' than in 3D in other respects as illustrated in Fig. 22. While the Kelvin–Helmholtz instability between the downflows and outflows is largely suppressed in 2D, this also implies that plumes of cold material can penetrate far into the neutrino-heated high-entropy bubbles provided that they develop in the first place. Because of the symmetry of the system, these plumes are actually toroidal structures, and can therefore completely constrict an outflow if they reach the symmetry axis (Fig. 22). Similarly, a downflow that wanders towards the pole can also constrict a polar outflow and cut it off from fresh supply of neutrino-heated material.

These events typically reduce the surface fraction covered by outflows at the recombination radius (where they start to contribute to the diagnostics explosion energy) for a considerable amount of time and thus reduce the rate of increase of $E_{\rm expl}$. Very often the explosion geometry changes dramatically after such an event and the surface fraction of the outflows remains small permanently. In some cases, a high-entropy bubble is cut off completely from the supply of neutrino-heated matter from below (Fig. 23) for several seconds. Even if an outflow is eventually re-established in the same direction, or if it is strong enough to survive because the cold plumes reach the axis at a relatively large radius (Fig. 22), the ejecta will then typically contain a large amount of cold material whose total net energy is barely positive, and the growth of the explosion energy will still be delayed. Such events explain excursions or even a permanent drop of the average total enthalpy $\bar{h}_{\rm tot}$ in the outflows to low values <0.3 in 2D (bottom panel of Fig. 12).

In 3D, the lack of symmetry as well as the Kelvin–Helmholtz instability prevents the constriction of outflows by cold plumes.

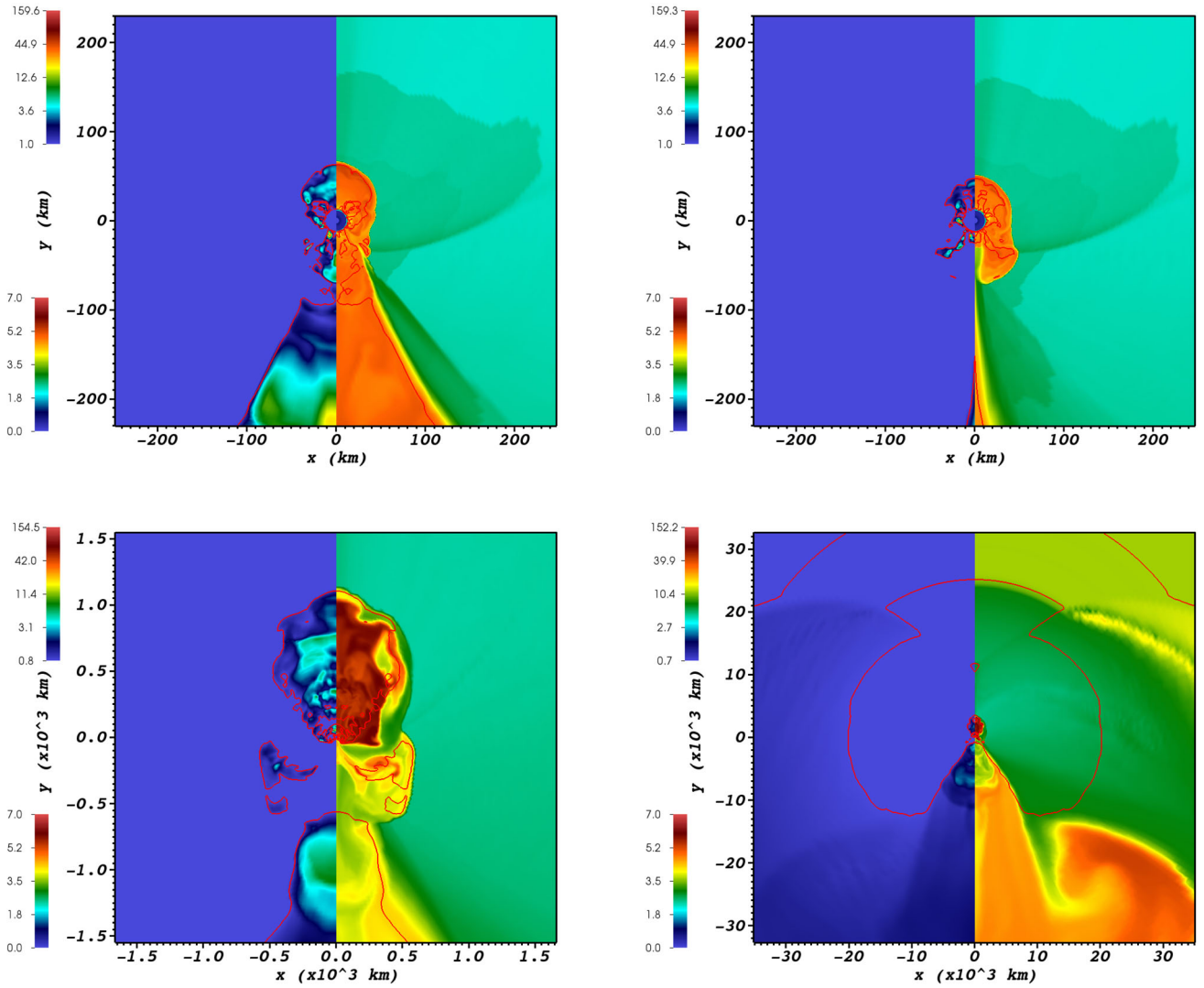

Figure 23. Snapshots of the radial velocity in units of 10^9 cm (left half of panels, lower colour bar) and the specific entropy s in k_b/nucleon (right half of panels, upper colour bar) depicting the separation of the high-entropy outflow from the gain region in model s11.6_2D and the re-establishment of an outflow after 'secondary shock revival' in model s11.0_2D. Red isovelocity contours are used to separate outward-moving matter with radial velocities larger than 10^7 cm s^{-1} from infalling matter. At 4.4 s (top left), matter is still being ejected in the Southern hemisphere, but at 4.5 s (top right) the outflow has become extremely thin, and matter in its wake starts falling back on to the neutron star. By 7.5 s (bottom left) a new outflow has developed in the Northern hemisphere, and the expansion of the secondary accretion shock in the Southern hemisphere stops further fallback from the outflow that was cut off earlier. By the end of the simulation at 8.2 s (bottom right), the newly formed bubble has expanded further to several thousands of kilometres in diameter. The post-shock velocities have become positive in all directions at this point, and only 0.035 $M_\odot$ in the downflows is still falling towards the proto-neutron star.

While the Kelvin–Helmholtz instability provides for some level of energy and momentum exchange between the accretion funnels and the expanding high-entropy bubbles as discussed in Section 5.2.1, it also prevents cold plumes from penetrating overly far into the neutrino-heated bubbles.

Mixing between downflows and outflows is thus not completely absent in 2D, it merely takes on a different guise and occurs only episodically, but with a more catastrophic effect than in 3D. Interestingly, there even appears to be an effect that compensates somewhat for the suppression of the Kelvin–Helmholtz instabilities in 2D due to the supersonic velocities in the downflows. Rayleigh–Taylor instabilities between the high-entropy bubbles and the cold overlying post-shock matter develop more readily in 2D. This is a natural consequence of higher entropies in the neutrino-heated bubbles in 2D (middle panel of Fig. 17), which implies a higher Atwood number between the bubbles and the colder post-shock matter. Thus, the lack of mixing by Kelvin–Helmholtz instabilities in 2D and the entropy boost due the dissipation of acoustic waves can also have a detrimental side effect on the robustness of the explosion.

5.2.5 Absence of a spherically symmetric neutrino-driven wind in 2D

In the most extreme cases of outflow constriction in 2D, the outflows are shut off altogether, and the outflow surface fraction drops to zero permanently, or at least over several seconds (bottom panel of Figs 21 and 23). This does not imply, however, that the explosion has failed; it only implies that neutrino heating is not strong enough to establish a wind that prevents the fallback of slowly moving matter in the wake of the shock. The pockets of cold, slowly moving

matter from the C/O shell in the 2D models that will undergo this kind of 'early fallback' (bottom-right panel of Fig. 23) only contain a few hundredths of a solar mass by the end of the simulations, and therefore will not change the neutron star mass considerably. Moreover, the mass accretion rate on to the secondary accretion shock is so low at late times that it can start to expand after 'secondary shock revival', thus re-establishing an outflow (bottom-right panel of Fig. 23).

While not indicative of a failure of the explosion, the small or vanishing outflow surface fraction in the long-time simulations none the less indicates [like the models of Bruenn et al. (2014)] that the separation of outgoing and infalling mass shells in 2D works differently from the usual picture where a high-entropy neutrino-driven wind with an approximately spherical flow geometry eventually develops. The polar outflows can be viewed as a confined wind driven jointly by neutrino heating and acoustic waves, but they never cover the entire sphere, and because of their flow geometry and the strong activity of acoustic waves, the outflow dynamics is completely different from spherical winds driven purely by neutrino heating.

From the foregoing, it is clear that the inhibition of the neutrino-driven wind in 2D is probably largely artificial, and we only mention this peculiarity for that reason. As discussed in Section 5.2.1, the presence of a larger effective eddy viscosity in 3D could terminate accretion earlier than in 2D (where supersonically infalling matter is hardly decelerated by lateral momentum transfer), or at least decelerate infalling matter sufficiently to be swept along by an incipient spherical wind after a few seconds. Moreover, our models likely underestimate the diffusive neutrino luminosity from the neutron star core and hence the neutrino heating at late times because we ignore the effect of nucleon correlations (Burrows & Sawyer 1998, 1999; Reddy et al. 1999), which shorten the proto-neutron star cooling time-scale considerably (Hüdepohl et al. 2010). It is conceivable that the concomitant increase of the wind mass-loss rate could still lead to a volume-filling outflow for more realistic neutrino opacities after a few seconds even in 2D.

5.2.6 *Reduced cooling due to 3D turbulence?*

Based on a successful supernova simulation of a $9.6\,M_\odot$ star, Melson et al. (2015b) recently suggested that the more efficient braking of the accretion downflows can be responsible for slightly higher explosion energies in 3D because the less violent impact of the downflows on the neutron star surface leads to reduced cooling. In our comparison of models s11.2_2Da and s11.2_3D, we observe some of the same symptoms noted by these authors, i.e. turbulent braking of the downflows and a reduced cooling rate $\dot{Q}_{\rm cool}$ at late times (Fig. 13). Obviously, this raises the question whether the mechanism proposed by Melson et al. (2015b) also operates in our 3D simulation, and how the physical processes we discussed so far in Sections 5.2.1–5.2.4 are related to it. Unfortunately, a comparison with Melson et al. (2015b) is not straightforward. While they found a sizeable increase of the explosion energy of 10 per cent in 3D compared to 2D, their explanation involved relatively tiny differences in some quantities (e.g. the gain radius and the temperature profiles in 2D and 3D) that cannot be confidently diagnosed in simulations like ours where the 2D and 3D models start to deviate from each other already shortly after bounce once prompt convection develops [which was not simulated by Melson et al. (2015b)]. None the less, there is sufficient evidence that we observe some rather different phenomena than Melson et al. (2015b).

Essentially, the mechanism proposed by Melson et al. (2015b) involves a *recession* of the gain radius in 3D compared to 2D due to reduced cooling to eject slightly more material in the explosion. Our simulations agree with Melson et al. (2015b) in showing a smaller volume-integrated cooling rate in 3D in the long term as accretion slowly subsides (Fig. 13).

However, we do not find a faster recession of the gain radius in 3D during the explosion phase (middle panel of Fig. 14), and the situation is ambiguous for the temperature at the gain radius $T_{\rm gain}$ (bottom panel of Fig. 14). In 3D, the temperature $T_{\rm gain}$ stagnates and falls below the 2D value around 250 ms at a time when the explosion is already considerably more vigorous in 3D than in 2D. We believe that the stagnation of $T_{\rm gain}$ is more indicative of the *slower* recession of the gain radius rather than of a higher cooling efficiency. The higher values of the Bernoulli integral and the total energy of the downflows at the gain radius in 3D (Figs 17 and 18) imply that there is actually more energy per unit mass available that can be radiated away in neutrinos as the accreted matter settles down in the cooling region.

Instead, the faster decline of the accretion rate on to the proto-neutron star in 3D is the dominant factor behind the lower cooling rate, making the lower cooling rate a *symptom rather than a cause* of the more vigorous explosion. Detailed comparisons would be required to check whether this true for the $9.6\,M_\odot$ model of Melson et al. (2015b) as well. Since outflow constriction is unlikely to happen for a model with robust shock expansion, the 2D/3D differences found by Melson et al. (2015b) as well as in the parametrize simulations of Handy et al. (2014) are probably most closely related to the different outflow efficiency in 2D and 3D, i.e. a more efficient 'rerouting' of freshly accreted matter into outflows. This tallies with their finding of a smaller surface filling factor of the downflows in 3D, which implies that a smaller fraction of the neutrino heating is wasted in regions where it cannot directly power an outflow. It also accounts for reduced mass accretion into the gain region and hence a recession of the gain radius in mass coordinate. While this mechanism is similar to the one discussed in Section 5.2.3 for our models, the effect is apparently smaller in the simulations of Melson et al. (2015b) because the accretion subsides fast enough to avoid the formation of secondary shocks and confined high-entropy bubbles in 2D, which can reduce the outflow efficiency by a factor of $\sim$2 in 2D.

Potentially, wave excitation at the convective boundary could also contribute to the 2D/3D differences in the simulations of Melson et al. (2015b). While they take reduced convective overshooting in 3D as an indication for reduced wave excitation, the effect probably plays a minor role in their case. The relatively small average speeds of the downflows at the gain radius ($\sim 10^8$ cm s^{-1} compared to $\sim 10^9$ cm s^{-1} in our model) are bound to make the excitation of g modes rather inefficient and thus rule them out as a major energy drain on the gain region in 2D. This is also suggested by the fact they find similar internal energies (and hence binding energies) in the outer regions of the cooling layer in 2D and 3D despite the stronger recession of the gain radius in 3D, which is quite different from what we discussed in Sections 5.2.1 and 5.2.2.

6 SUMMARY AND CONCLUSIONS

We have presented a successful 3D GR simulation of the explosion of an $11.2\,M_\odot$ star using the FMT multi-group transport scheme of Müller & Janka (2015). The model has been evolved to almost 1 s after bounce, and has reached a diagnostic explosion energy of 1.3×10^{50} erg at that point, which is still growing by the end of the

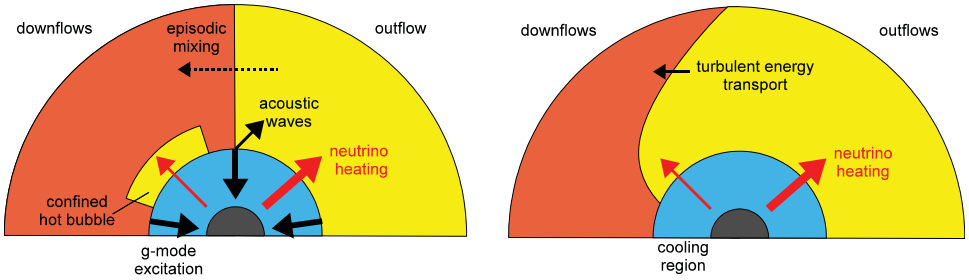

Figure 24. Sketch of the different energy budget between the outflows (yellow), the downflows (red), and the cooling region (blue) in 2D (left) and 3D (right). In 3D, turbulent eddy diffusivity leads to a persistent, small energy flux (short solid arrow) from the neutrino-heated outflows to the downflows, whereas mixing between the outflows and downflows only occurs episodically in 2D, but has more dramatic consequences in this case because it leads to large-scale mixing of cold matter into the outflows (long dotted arrow). There is a considerable energy transfer from the gain region to the cooling region due to wave excitation in 2D and an indirect transfer of energy from the downflows to the gain region by the excitation of acoustic waves in 2D (which can lead to larger asymptotic energies per unit mass in the ejecta); this is absent in 3D. Moreover, a considerable amount of neutrino heating (red arrows) is wasted in 2D because it is deposited in confined bubbles, whereas almost the entire neutrino heating in 3D is used to lift matter out of the gravitational well.

simulation. The baryonic neutron star mass $M_{\rm by}$ at the end of the simulations has reached 1.33 $\mathrm{M}_\odot$ and estimates of the final neutron star mass yield $M_{\rm by} \approx 1.41$–$1.48\,\mathrm{M}_\odot$ and a gravitational mass not exceeding $1.34\,\mathrm{M}_\odot$, which is compatible with the measured neutron star mass distribution (Schwab et al. 2010). The fact that we obtain an explosion for this progenitor with a relatively accurate multi-group transport scheme further illustrates that even the non-exploding state-of-the-art models (Hanke et al. 2013; Tamborra et al. 2014a,b) with the best available neutrino transport and microphysics are apparently very close to shock revival, something which is also suggested by the recent successful 3D explosion models of the Garching (Melson et al. 2015a,b) and Oakridge groups (Lentz et al. 2015).

A comparison of the explosion dynamics after shock revival with 2D long-time simulations of different progenitors with ZAMS masses between 11.0 and $11.6\,\mathrm{M}_\odot$ revealed a faster and more stable growth of the explosion energy in 3D compared to 2D. Because accretion downflows and neutrino-driven outflows coexist over several seconds in 2D, the explosion energy in the 2D models can still reach values of up to 2×10^{50} erg, but this comes at the expense of high neutron star masses ($M_{\rm by} \gtrsim 1.6\,\mathrm{M}_\odot$) that are likely incompatible with the observed neutron star mass distribution. A detailed comparison of the 2D and 3D models unearthed several physical mechanisms responsible for the more robust rise of the explosion energy in 3D and the slower growth of the proto-neutron star mass, which is a symptom of the faster subsidence of accretion. The specific effects that we find are summarized below, and we also provide a schematic visualization of the different flow geometry and the energy budget of the downflows, the outflows, and the gain region in Fig. 24 to aid the reader's understanding.

(1) In 2D, the interfaces between the accretion funnels and the neutrino-heated bubbles tend to become laminar after shock revival, while they are corrugated by the Kelvin–Helmholtz instability in 3D. We ascribe the different behaviour to the suppression of the purely two-dimensional modes of the Kelvin–Helmholtz instability in the supersonic regime (Gerwin 1968). The effect is thus distinct from the inverse turbulent energy cascade in 2D (Kraichnan 1967), which has been invoked as an explanation for the different behaviour of 2D and 3D models prior to shock revival, since the different energy cascade in 2D and 3D is not related to the Mach number of the flow.

(2) As a consequence, the effective eddy viscosity and diffusivity between the downflows and outflows is larger in 3D than in 2D during most phases, i.e. there is more exchange of energy and momentum between the outflows and downflows. On the one hand, this implies that the outflows contribute only ∼6 MeV/nucleon to the explosion energy in 3D, as some of the net total (i.e. thermal+kinetic+potential) energy gained from nucleon recombination of ∼8.8 MeV/nucleon is lost to the downflows by turbulent diffusion. On the other hand, the turbulence effectively 'brakes' the downflows, and they arrive at the gain radius with smaller velocities but higher total energy per unit mass than in 2D.

(3) The higher impact velocities of the downflows and the formation of secondary accretion shocks at small radii in 2D lead to a more efficient excitation of g modes and acoustic waves at the gain radius that transport energy into deeper regions of the cooling layer and into the neutrino-heated ejecta, respectively. Our analysis suggests that the energy loss from the gain region by wave excitation becomes comparable to the volume-integrated neutrino heating rate at late times, and by increasing the absolute value of the binding energy $|e_{\rm tot}|$ at the gain radius significantly reduces the mass outflow rate that can be sustained by neutrino heating. In 3D, the turbulent energy flux into the gain region is small, and the binding energy at the gain radius is smaller by factor of $\gtrsim$2 at late times, which allows for a higher mass outflow rate than in 2D. The dissipation of acoustic waves in the outflows in 2D provides only for a partial 'recycling' of the energy lost by wave excitation, but can increase the total energy per unit mass in the outflows to values larger than the recombination energy of 8.8 MeV/nucleon.

(4) In addition, the outflow efficiency $\eta_{\rm out} = \dot{M}_{\rm out}/(\dot{Q}_{\rm heat}/|e_{\rm gain}|)$ is also higher in 3D ($\eta_{\rm out} \sim 1$ with strong fluctuations) than in 2D ($\eta_{\rm out} \lesssim 0.5$ at late times), i.e. for a given amount of neutrino heating and a given binding energy at the gain radius, more mass is channelled into outflows and contributes to the explosion energy in 3D. The low outflow efficiency in 2D stems from the large surface fraction occupied by fast downflows and 'confined bubbles' between downflows whose expansion is inhibited by the formation of secondary accretion shocks.

(5) Episodic mixing between the outflows and downflows still occurs in 2D, e.g. by the formation of new downflows as a result of the Rayleigh–Taylor between the cold shocked material and the neutrino-heated high-entropy bubbles. While mixing only occurs sporadically in 2D, the consequences of these mixing events are more catastrophic than in 3D. Not only do they slow down the rise of the explosion energy by mixing cold material into the outflows; the penetration of accretion funnels into the high-entropy bubbles can also lead to the constriction of outflows, sometimes shutting

them off completely and permanently decreasing the outflow surface fraction to values of $\lesssim 0.3$.

Our simulations thus provide ample evidence that 3D effects can play a beneficial role in core-collapse supernova explosions *after* shock revival. However, since our current 3D model has only been evolved to ∼1 s after bounce and does not yet permit us to deduce the final explosion and remnant properties directly because of continuing accretion (and forced us to resort to indirect arguments about the final neutron star masses), a number of open questions remain and invite speculation. Moreover, limited conclusions can be drawn from a single 3D simulation of one progenitor. Given the recent progress on other fronts in supernova theory, the questions and perspectives for future research on the role of 3D effects during the explosion phase can be summarized as follows.

(1) Longer 3D simulations with higher resolution are necessary to determine final explosion energies, nickel masses, and neutron star masses precisely for comparison with observations without recourse to indirect methods. Our estimate for the final baryonic neutron star mass of $1.48\,M_\odot$ for the 3D model of the $11.2\,M_\odot$ progenitor still assumes the accretion of an additional $0.15\,M_\odot$, which is much more than a visual inspection of Fig. 10 suggests given the very slow rise of the neutron star mass in 3D. If the turbulent braking of the downflows terminates accretion before the post-shock velocity equals the escape velocity as speculated in Section 5.2.1, the final baryonic and gravitational neutron star mass might be as low as ∼1.35 and $\sim 1.24\,M_\odot$, respectively. This would indicate that a plausible distribution of neutron star masses spanning the entire range of observed values down to the lower end is within reach of modern multi-D simulations of neutrino-driven supernovae.

(2) A more rigorous analysis of the turbulent multi-dimensional flow in the spirit of Reynolds decomposition would be highly desirable in order to further bolster our qualitative interpretation of 3D effects in the post-explosion phase. Such quantitative analysis methods have considerably advanced our understanding of the turbulent flow during the accretion phase (Murphy & Meakin 2011). After shock revival, the non-stationarity of the flow presents a challenge for such methods, however. Our relatively crude two-stream analysis based on a separation of the outflows and downflows could also be improved in order to account more directly and rigorously for the turbulent exchange of mass, momentum, and energy between the two streams, but such an analysis faces a major challenge in the form of the complicated flow geometry.

(3) Whether and to what extent the positive 3D effects described in this paper come into play obviously depends on whether shock revival can be accomplished in 3D in the first place and on the delay compared to the 2D case. If there is a significant delay in shock revival, 3D models may not be able to equalize the 'head start' of the 2D models at least of relatively powerful explosions where the diagnostic energy shows first signs of levelling off after ∼300 ms or less (Bruenn et al. 2014; Pan et al. 2015). Even in this case, the mechanism discussed in this paper could none the less help to mitigate the 'penalty' incurred by the delay of the explosion in 3D and allow the models to remain compatible with observational constraints. Moreover, if accretion lasts longer – as in the 2D simulations of Müller et al. (2012a,b) and Janka et al. (2012) – the beneficial 3D effects in the phase after shock revival may outweigh the 'penalty' of delayed shock revival. Furthermore, it is conceivable that the problem of missing or delayed explosion in 3D may yet be resolved by the inclusion of better, multi-dimensional progenitor models with large-scale initial perturbations that aid shock revival (Couch & Ott 2013, 2015; Müller & Janka 2015), unknown microphysics (Melson et al. 2015a). Strongly SASI-dominated models may even explode more easily in 3D (Fernández 2015).

(4) The robustness of the mechanisms described in this paper needs to be studied further for a wider range of progenitors. The 2D simulations (Buras et al. 2006b; Müller et al. 2012a) of the $11.2\,M_\odot$ progenitor considered here have been particularly noteworthy examples for suspiciously low explosion energies and long-lasting accretion. This behaviour is due to the specific characteristics of progenitors around $11\,M_\odot$, including a relatively small silicon core and a very pronounced density jump at the Si/SiO interface. These properties result in a small proto-neutron star mass M immediately after shock revival and hence low neutrino energies [cp. the scaling of the electron antineutrino energy with M found by Müller & Janka (2014)] as well as a small accretion luminosity. Both of these factors contribute to relatively weak neutrino heating after shock revival and a small mass outflow rate. The tepid nature of our 2D explosions may thus hinge very much on the peculiar structure of low-mass supernova progenitors.

It therefore remains to be seen whether 3D effects provide a similarly strong boost for the growth of the explosion energy in other progenitors. Whenever 2D models develop the characteristic broad downflows and secondary shocks indicative of long-lasting accretion during a relatively weak explosion, such as the 15 and $27\,M_\odot$ models of Müller et al. (2012a) and Janka et al. (2012), the physical mechanisms identified here likely come into play eventually. On the other hand, they may play a negligible role if the volume fraction of the downflows drops very quickly as in the models of Bruenn et al. (2014) and Lentz et al. (2015) or the parametrized models of Handy et al. (2014). Since 2D supernova simulations of different groups have not yet converged sufficiently to decide whether there is a generic problem of 'weak explosions' in 2D, it is impossible to judge the generic character of our findings. By the same token, however, it cannot be ruled out that 2D models *should be* generically underenergetic and overestimate the amount of accretion after shock revival due to the mechanisms we identified, and that realistic explosion energies and remnant masses will only be obtained in 3D. If so, prematurely confronting the 2D models with the observational constraints could lead to wrong conclusions.

Thus, more work is necessary to substantiate the intriguing perspective that 3D effects could help to achieve agreement between simulations of neutrino-driven supernovae and observational constraints such as explosion energies and neutron star masses. Far from offering a complete solution due to the limitations of computational resources that have always plagued supernova theory, our present study can only take a first step in this direction and adumbrate some of the physical mechanisms that could help to boost 3D explosions after shock revival. None the less, even our current results already serve an antidote against undue pessimism after initial setbacks in 3D multi-group neutrino hydrodynamics simulations. Along with the recent successful explosions in first-principle models, the identification of other beneficial effects of the third dimension on the explosion threshold and energetics, and plausible ideas for solving the problem of missing explosions with the help of multi-D progenitor models and/or non-standard microphysics, they are another piece that fits well into the overall puzzle, suggesting that a solution for the supernova problem is slowly taking shape.

ACKNOWLEDGEMENTS

The author acknowledges fruitful exchange with H. Andressen, A. Burrows, Th. Foglizzo, A. Heger, W.R. Hix, H.-Th. Janka, Y. Levin,

T. Plewa, and T. Waters. He has been supported by the Australian Research Council through a Discovery Early Career Researcher Award (grant DE150101145) and by the Alexander von Humboldt Foundation through a Feodor Lynen fellowship. The computations were performed on *Raijin* at the NCI National Facility (project fh6) using computer time contingents obtained through NCMAS, ASTAC, and a Monash LIEF top-up grant, on the Monash eGrid Cluster, and on the IBM iDataPlex system *hydra* at the Rechenzentrum of the Max-Planck Society (RZG).

REFERENCES

Abdikamalov E. et al., 2014, ApJ, preprint (arXiv:1409.7078)
Arnett D., 1994, ApJ, 427, 932
Arnett W. D., Meakin C., 2011, ApJ, 733, 78
Asida S. M., Arnett D., 2000, ApJ, 545, 435
Balsa T. F., Goldstein M. E., 1990, J. Fluid Mech., 216, 585
Banyuls F., Font J. A., Ibanez J. M. A., Martí J. M. A., Miralles J. A., 1997, ApJ, 476, 221
Bazan G., Arnett D., 1994, ApJ, 433, L41
Bazan G., Arnett D., 1998, ApJ, 496, 316
Blondin J. M., Mezzacappa A., DeMarino C., 2003, ApJ, 584, 971
Blumen W., 1970, J. Fluid Mech., 40, 769
Blumen W., Drazin P. G., Billings D. F., 1975, J. Fluid Mech., 71, 305
Boyd J. P., 2001, Chebyshev and Fourier Spectral Methods, 2nd ed. Dover Press, New York
Bruenn S. W., 1985, ApJS, 58, 771
Bruenn S. W. et al., 2013, ApJ, 767, L6
Bruenn S. W. et al., 2014, preprint (arXiv:1409.5779)
Buras R., Rampp M., Janka H.-T., Kifonidis K., 2006a, A&A, 447, 1049
Buras R., Janka H.-T., Rampp M., Kifonidis K., 2006b, A&A, 457, 281
Burrows A., 2013, Rev. Mod. Phys., 85, 245
Burrows A., Fryxell B. A., 1992, Science, 258, 430
Burrows A., Goshy J., 1993, ApJ, 416, L75
Burrows A., Sawyer R. F., 1998, Phys. Rev. C, 58, 554
Burrows A., Sawyer R. F., 1999, Phys. Rev. C, 59, 510
Burrows A., Hayes J., Fryxell B. A., 1995, ApJ, 450, 830
Burrows A., Livne E., Dessart L., Ott C. D., Murphy J., 2006, ApJ, 640, 878
Burrows A., Livne E., Dessart L., Ott C. D., Murphy J., 2007, ApJ, 655, 416
Cerdá-Durán, 2009, Mesh Coarsening in Relativistic Hydrodynamics, http://www.mpa-garching.mpg.de/hydro/COCONUT/valencia2009/Talks/Cerda-Duran.pdf
Choudhury S. R., Lovelace R. V. E., 1984, ApJ, 283, 331
Chugai N. N., Utrobin V. P., 2014, Astron. Lett., 40, 291
Colella P., Woodward P. R., 1984, J. Comput. Phys., 54, 174
Cordero-Carrión I., Cerdá-Durán P., Dimmelmeier H., Jaramillo J. L., Novak J., Gourgoulhon E., 2009, Phys. Rev. D, 79, 024017
Couch S. M., 2013a, ApJ, 765, 29
Couch S. M., 2013b, ApJ, 775, 35
Couch S. M., O'Connor E. P., 2014, ApJ, 785, 123
Couch S. M., Ott C. D., 2013, ApJ, 778, L7
Couch S. M., Ott C. D., 2015, ApJ, 799, 5
Couch S. M., Chatzopoulos E., Arnett W. D., Timmes F. X., 2015, ApJL, preprint (arXiv:1503.02199)
Dimmelmeier H., Font J. A., Müller E., 2002, A&A, 388, 917
Dolence J. C., Burrows A., Murphy J. W., Nordhaus J., 2013, ApJ, 765, 110
Drazin P. G., Davey A., 1977, J. Fluid Mech., 82, 255
Fernández R., 2015, MNRAS, preprint (arXiv:1504.07996)
Foglizzo T., Galletti P., Scheck L., Janka H.-T., 2007, ApJ, 654, 1006
Fragile P. C., Lindner C. C., Anninos P., Salmonson J. D., 2009, ApJ, 691, 482
Gerwin R. A., 1968, Rev. Mod. Phys., 40, 652
Goldreich P., Kumar P., 1990, ApJ, 363, 694
Guilet J., Foglizzo T., 2012, MNRAS, 421, 546
Handy T., Plewa T., Odrzywołek A., 2014, ApJ, 783, 125
Hanke F., 2014, PhD thesis, Technische Universtiät München
Hanke F., Marek A., Müller B., Janka H.-T., 2012, ApJ, 755, 138
Hanke F., Müller B., Wongwathanarat A., Marek A., Janka H.-T., 2013, ApJ, 770, 66
Herant M., Benz W., Colgate S., 1992, ApJ, 395, 642
Herant M., Benz W., Hix W. R., Fryer C. L., Colgate S. A., 1994, ApJ, 435, 339
Hüdepohl L., 2014, PhD thesis, Technische Universtiät München
Hüdepohl L., Müller B., Janka H., Marek A., Raffelt G. G., 2010, Phys. Rev. Lett., 104, 251101
Janka H.-T., 2012, Annu. Rev. Nucl. Part. Sci., 62, 407
Janka H.-T., Müller E., 1996, A&A, 306, 167
Janka H.-T., Hanke F., Hüdepohl L., Marek A., Müller B., Obergaulinger M., 2012, Prog. Theor. Exp. Phys., 2012, 010000
Kageyama A., Sato T., 2004, Geochem. Geophys. Geosyst., 5, Q09005
Kifonidis K., Plewa T., Janka H.-T., Müller E., 2003, A&A, 408, 621
Klimishin I. A., Gnatyk B. I., 1981, Astrophysics, 17, 306
Koldoba A. V., Romanova M. M., Ustyugova G. V., Lovelace R. V. E., 2002, ApJ, 576, L53
Kompaneets A. S., 1960, Sov. Phys. Dokl., 5, 46
Koo B.-C., McKee C. F., 1990, ApJ, 354, 513
Kraichnan R. H., 1967, Phys. Fluids, 10, 1417
Kuhlen M., Woosley W. E., Glatzmaier G. A., 2003, in Turcotte S., Keller S. C., Cavallo R. M., eds, ASP Conf. Ser. Vol. 293, 3D Stellar Evolution. Astron. Soc. Pac., San Francisco, p. 147
Laming J. M., 2007, ApJ, 659, 1449
Lattimer J. M., Swesty F. D., 1991, Nucl. Phys. A, 535, 331
Laumbach D. D., Probstein R. F., 1969, J. Fluid Mech., 35, 53
Lecoanet D., Quataert E., 2013, MNRAS, 430, 2363
Lentz E. J., Mezzacappa A., Bronson Messer O. E., Liebendörfer M., Hix W. R., Bruenn S. W., 2012a, ApJ, 747, 73
Lentz E. J., Mezzacappa A., Bronson Messer O. E., Hix W. R., Bruenn S. W., 2012b, ApJ, 760, 94
Lentz E. J. et al., 2015, ApJL, preprint (arXiv:1505.05110)
Malamud G. et al., 2013, High Energy Density Phys., 9, 672
Marek A., Janka H., 2009, ApJ, 694, 664
Marek A., Janka H., Müller E., 2009, A&A, 496, 475
Matzner C. D., McKee C. F., 1999, ApJ, 510, 379
Meakin C. A., Arnett D., 2006, ApJ, 637, L53
Meakin C. A., Arnett D., 2007a, ApJ, 665, 690
Meakin C. A., Arnett D., 2007b, ApJ, 667, 448
Melson T., Janka H.-T., Bollig R., Hanke F., Marek A., Mueller B., 2015a, preprint (arXiv:1504.07631)
Melson T., Janka H.-T., Marek A., 2015b, ApJ, 801, L24
Mignone A., Bodo G., 2005, MNRAS, 364, 126
Müller E., Janka H.-T., 1997, A&A, 317, 140
Müller B., Janka H.-T., 2014, ApJ, 788, 82
Müller B., Janka H.-T., 2015, MNRAS, 448, 2141
Müller B., Janka H., Dimmelmeier H., 2010, ApJS, 189, 104
Müller B., Janka H.-T., Marek A., 2012a, ApJ, 756, 84
Müller B., Janka H.-T., Heger A., 2012b, ApJ, 761, 72
Müller B., Janka H.-T., Marek A., 2013, ApJ, 766, 43
Murphy J. W., Burrows A., 2008, ApJ, 688, 1159
Murphy J. W., Meakin C., 2011, ApJ, 742, 74
Murphy J. W., Ott C. D., Burrows A., 2009, ApJ, 707, 1173
Murphy J. W., Dolence J. C., Burrows A., 2013, ApJ, 771, 52
Nakamura K., Kuroda T., Takiwaki T., Kotake K., 2014, ApJ, 793, 45
Obergaulinger M., Janka H.-T., Aloy M. A., 2014, MNRAS, 445, 3169
Pan K.-C., Liebendörfer M., Hempel M., Thielemann F.-K., 2015, ApJL, preprint (arXiv:1505.02513)
Pejcha O., Prieto J. L., 2015, ApJ, 806, 225
Perego A., Hempel M., Fröhlich C., Ebinger K., Eichler M., Casanova J., Liebendoerfer M., Thielemann F.-K., 2015, ApJ, 806, 275
Poznanski D., 2013, MNRAS, 436, 3224
Rampp M., Janka H.-T., 2002, A&A, 396, 361
Reddy S., Prakash M., Lattimer J. M., Pons J. A., 1999, Phys. Rev. C, 59, 2888
Ronchi C., Iacono R., Paolucci P. S., 1996, J. Comput. Phys., 124, 93
Scheck L., Kifonidis K., Janka H.-T., Müller E., 2006, A&A, 457, 963
Schwab J., Podsiadlowski P., Rappaport S., 2010, ApJ, 719, 722

Sedov L. I., 1959, Similarity and Dimensional Methods in Mechanics. Academic Press, New York
Suwa Y., Kotake K., Takiwaki T., Whitehouse S. C., Liebendörfer M., Sato K., 2010, PASJ, 62, L49
Suwa Y., Takiwaki T., Kotake K., Fischer T., Liebendörfer M., Sato K., 2013, ApJ, 764, 99
Takiwaki T., Kotake K., Suwa Y., 2014, ApJ, 786, 83
Tamborra I., Raffelt G., Hanke F., Janka H.-T., Müller B., 2014a, Phys. Rev. D, 90, 045032
Tamborra I., Hanke F., Janka H.-T., Müller B., Raffelt G. G., Marek A., 2014b, ApJ, 792, 96
Tanaka M. et al., 2009, ApJ, 692, 1131
Thompson C., 2000, ApJ, 534, 915
Timmes F. X., Woosley S. E., Weaver T. A., 1996, ApJ, 457, 834
Utrobin V. P., Chugai N. N., 2011, A&A, 532, A100
van Leer B., 1977, J. Comput. Phys., 23, 263
Weinberg N. N., Quataert E., 2008, MNRAS, 387, L64
Wilson J. R., Mayle R. W., 1988, Phys. Rep., 163, 63
Wongwathanarat A., Hammer N. J., Müller E., 2010, A&A, 514, A48
Wongwathanarat A., Müller E., Janka H.-T., 2015, A&A, 577, A48
Woosley S. E., Weaver T. A., 1995, ApJS, 101, 181
Woosley S. E., Heger A., Weaver T. A., 2002, Rev. Mod. Phys., 74, 1015
Yakunin K. N. et al., 2010, Class. Quantum Grav., 27, 194005
Zink B., Schnetter E., Tiglio M., 2008, Phys. Rev. D, 77, 103015

APPENDIX: DEFINITION OF ENERGIES AND ENERGY FLUXES IN GENERAL RELATIVITY

While the computation of mass fluxes and spherically averaged profiles of hydrodynamic quantities can be readily generalized to the relativistic case just by including the correct three-volume element, the definition of energies and energy fluxes in the relativistic case is less straightforward, and is therefore briefly expounded in this appendix. We use geometric units ($G = c = 1$) throughout this section.

After adopting a 3 + 1 foliation of space–time and projecting the components of the stress–energy tensor into components orthogonal and parallel to the 3-hypersurfaces, the energy equation in GR hydrodynamics can be written in the formulation of Banyuls et al. (1997) in terms of a new conserved variable τ as

$$\frac{\partial\sqrt{\gamma}\tau}{\partial t}+\frac{\partial\sqrt{-g}\left(\tau\hat{v}^i+Pv^i\right)}{\partial x^i}=\alpha\sqrt{-g}\left(T^{\mu 0}\frac{\partial\ln\alpha}{\partial x^\mu}-T^{\mu\nu}\Gamma^0_{\mu\nu}\right). \tag{A1}$$

Here, τ is defined in terms of the baryonic mass density ρ in the fluid frame, the Lorentz factor W, the internal energy density ϵ (including all rest-mass contributions), the pressure P, and the relativistic enthalpy $h = 1 + \epsilon + P/\rho$ as

$$\tau=\rho hW^2-P-\rho W=\rho(1+\epsilon+P/\rho)W^2-P-\rho W. \tag{A2}$$

Furthermore, γ and g are the determinants of the three- and four-metric, respectively, and the advection term contains $\hat{v}^i = v^i - \beta^i/\alpha$ instead of the Eulerian three-velocity v^i. By pushing the lapse function α into the temporal and spatial derivatives, it is possible to formulate a strict conservation law (without a source term) analogous to the limit of a stationary space–time with a zero shift vector (cp. equation A35 in Müller et al. 2010, where the right-hand side reduces to zero in this limit):

$$\frac{\partial}{\partial t}\left[\sqrt{\gamma}\alpha\left(\tau+D\right)-\sqrt{\gamma}D\right]+\frac{\partial}{\partial x^i}\left[\sqrt{-g}\left(\alpha\tau\hat{v}^i+\alpha D\hat{v}^i-D\hat{v}^i+\alpha Pv^i\right)\right]=0. \tag{A3}$$

Here, we have introduced the baryonic mass density in the Eulerian frame $D = \rho W$ to simplify the equation.

This suggests that in the limit of a vanishing shift vector and a stationary metric, the Newtonian expression $e_{\rm tot} = \epsilon + \boldsymbol{v}^2/2 + \Phi$ for the total energy per unit mass (including rest-mass contributions) can be generalized to

$$e_{\rm tot,rm}=\frac{\alpha\tau}{D}+(\alpha-1), \tag{A4}$$

and the role of the total Newtonian enthalpy in the flux is taken by

$$h_{\rm tot,rm}=\alpha\tau/D+(\alpha-1)+\alpha P/D. \tag{A5}$$

It is noteworthy that the internal energy and rest-mass contributions (which enter the equations through τ) always appear in conjunction with factors W and α. Strictly speaking, it is therefore no longer possible to formulate the energy equation in general relativity without including rest-mass contributions in the conserved quantities and the fluxes by pushing them into a nuclear source term instead (as least not in a simple form). Computing fluxes and total energies excluding rest-mass contributions is therefore somewhat less meaningful in general relativity. However, since we have $\alpha \approx 1$ and $v \lesssim 0.3c$ in the gain region, the higher order relativistic corrections are small enough to be neglected, it is still reasonable to compute total energies and enthalpies without rest-mass contributions by using just the thermal energy contribution $\epsilon_{\rm therm}$ to the internal energy density ϵ instead of $\epsilon = \epsilon_{\rm therm} + \epsilon_{\rm rm}$.

For the other quantities, considered in this paper, the generalization is trivial. Mass fluxes through the surface of a sphere or parts of it are computed as

$$\dot{M}=\int\alpha Dv_{\rm r}r^2\phi^4\,{\rm d}\Omega, \tag{A6}$$

where $v_{\rm r}$ is the radial velocity component measured in the orthonormalized Eulerian frame and ϕ is the conformal factor in the xCFC metric, and the computation of energy/enthalpy fluxes works analogously. The density-weighted spherical average $\bar{X}$ of a quantity X is computed as

$$\bar{X}=\frac{\int DX\phi^4\,{\rm d}\Omega}{\int D\phi^4\,{\rm d}\Omega}. \tag{A7}$$

This paper has been typeset from a TEX/LATEX file prepared by the author.